Stark structure of the Rydberg states of alkali-metal atoms

Myron L. Zimmerman, Michael G. Littman, Michael M. Kash, and Daniel Kleppner
Research Laboratory of Electronics and Department of Physics, Massachusetts Institute of Technology, Cambridge, Massachusetts 02139
(Received 21 May 1979)

The authors describe practical methods for calculating the Stark structure of Rydberg states of the alkali metals based on diagonalization of the energy matrix. A survey of Stark structures is presented for all of the alkali metals in the vicinity of $n = 15$. Topics discussed include general methods for evaluating radial matrix elements, the treatment of fine structure, oscillator-strength distribution, scaling laws, the structure of a level anticrossing, and sources of error. Experimental Stark maps are compared with calculated results for lithium and cesium. Experimental studies of the oscillator-strength distribution within a Stark manifold and the structure of a level anticrossing are also presented.

I. INTRODUCTION

The growing study of highly excited atoms has renewed interest in the behavior of atoms in electric fields. As the principle quantum number n increases, the size of the orbit, and hence the coupling of the electron with an applied electric field, increases as n^2, whereas the binding energy decreases as n^{-2}. Ultimately the Stark interaction can dominate the level structure of the atom, even for modest fields. Thus the eigenstates in an electric field constitute the most useful basis for describing the system, and understanding these states clearly is a prerequisite for carrying out many studies of highly excited atoms. In this paper we describe methods for efficiently calculating the energy levels (Stark structure) of Rydberg states of the alkali metals or other one-electron atoms and we present a survey of the Stark structure of each of the alkali metals. The calculations are compared with experiment for two alkali metals, lithium and cesium.

To set the stage it is important to realize that perturbative treatments of the energy employing power-series expansions in the field are fundamentally inadequate. Such treatments, for example, are poorly suited for describing an anticrossing between levels of different terms and fail hopelessly when several anticrossings occur. (There is one important exception to this generalization: in a pure Coulomb potential, levels from different terms actually cross and perturbation theory works well.) Furthermore, each atom turns out to be a special case. As we shall see, it is possible to make some predictions about how the Stark structure is affected if, say, a single angular-momentum eigenstate is shifted in energy. On the other hand, if several states are shifted the results are full of surprises, with unexpected repulsions between certain levels and apparent crossings between others. Consequently, we have chosen to present our results in what is essentially an atlas of maps of the Stark structure of the alkali metals, accompanied by a description of how to calculate the Stark structure of other one-electron systems. For reasons which will be discussed below, we have chosen to concentrate on the region about $n = 15$.

In Sec. II we review general features of the Stark structure of hydrogen. Section III contains a discussion of calculational methods for the Stark structure of one-electron atoms and in Sec. IV sources of error are described. A brief summary of the experimental techniques which were employed to observe the Stark structure is given in Sec. V. The calculated and observed Stark maps are presented in Sec. VI. In Sec. VII level crossings and anticrossings are examined and in Sec. VIII we present some concluding remarks.

II. BACKGROUND

Because alkali Rydberg states are hydrogenlike in many respects, the Stark structure of hydrogen provides a natural starting point for our discussion. Schrödinger's equation for hydrogen in a static electric field, neglecting electron and nuclear spin, is

$$(-\tfrac{1}{2}\nabla^2 - 1/r + Fz)\Psi(\vec{r}) = W\Psi(\vec{r}) . \quad (1)$$

(Atomic units are used unless otherwise indicated.) W is the energy and F is the magnitude of the electric field which is taken to lie along the z axis. Equation (1) is separable in parabolic coordinates[1] and can be solved analytically for $F = 0$. The quantum numbers n, n_1, n_2, and $|m|$ label the states, where n and m are the principle and "magnetic" quantum numbers, respectively, and n_1 and n_2 are non-negative integers which obey

$$n_1 + n_2 + |m| + 1 = n . \quad (2)$$

Silverstone[2] has applied a general method for

carrying out perturbation theory to any order in the field and has evaluated the expansion through twenty-fifth order. The leading terms are

$$W_0 = -1/2n^2 , \tag{3a}$$

$$W_1 = \tfrac{3}{2}n(n_1 - n_2)F , \tag{3b}$$

$$W_2 = -\tfrac{1}{16}n^4[17n^2 - 3(n_1 - n_2)^2 - 9m^2 + 19]F^2 , \tag{3c}$$

$$W_3 = \tfrac{3}{32}n^7(n_1 - n_2)[23n^2 - (n_1 - n_2)^2 + 11m^2 + 39]F^3 , \tag{3d}$$

$$\begin{aligned} W_4 = -\tfrac{1}{1024}n^{10}[&5487n^4 + 35182n^2 - 1134m^2(n_1 - n_2)^2 \\ &+ 1806n^2(n_1 - n_2)^2 - 3402n^2m^2 + 147(n_1 - n_2)^4 \\ &- 549m^2 + 5754(n_1 - n_2)^2 - 8622m^2 + 16211]F^4 . \end{aligned} \tag{3e}$$

Unfortunately, the perturbation expansion is asymptotic and nonconvergent. In low fields it is well behaved, however, and yields a good estimate of the real energy eigenvalue provided that one does not carry the expansion too far.[3] In fields below the ionization threshold for alkali metals[4] (i.e., $F < W^2/4$), the perturbation expansion is valid to at least fourth order. When testing our calculations against perturbation theory we shall drop terms higher than fourth order. This introduces an error which is usually smaller than the fourth-order term, and in most cases is below our level of accuracy.

From Eqs. (3) we can obtain the global features of the Stark structure of hydrogen. The zeroth-order term provides a natural unit, the separation between adjacent principle levels:

$$\Delta W_0 \equiv W_0(n+1) - W_0(n) \cong 1/n^3 . \tag{4}$$

The first-order term, Eq. (3b), reveals that for a given $|m|$ the adjacent Stark levels are separated by

$$\Delta W_1 \equiv W_1(n, n_1, |m|) - W_1(n, n_1 - 1, |m|) = 3nF . \tag{5}$$

The location of the first crossing between levels of different terms (i.e., between the highest level of n and the lowest level of $n+1$) occurs at the field

$$F \cong 1/3n^5 . \tag{6}$$

Such crossings appear to violate the "no-crossing" theorem, but this is not the case: The Coulomb potential possesses a dynamical symmetry which allows levels of identical m to cross.[5] In alkali metals this symmetry is broken by the core, and levels with the same value of m generally cannot cross.

III. METHOD

A. General procedure

An alkali-metal-atom valence electron can be described for our purposes by the single-particle Hamiltonian

$$\mathcal{H} = -\tfrac{1}{2}\nabla^2 + V(r) + Fz . \tag{7}$$

Effects of electron and nuclear spin as well as valence-core electron correlation are small and neglected, although we shall introduce fine structure later since it is experimentally important for the heavier alkali metals.

Because $V(r)$ is not precisely known and $\mathcal{H}$ is not separable, analytic solutions to the Stark problem are not possible. As discussed above, perturbation theory is not suited to calculating Stark structure. Precise approximation methods are possible, however, based on the following considerations: Outside of the electron core, $V(r)$ is essentially Coulombic. Thus, in the absence of the applied field, accurate wave functions can be constructed for this spatial region which have the correct energies and which vanish as $r \to \infty$. Matrix elements for operators which weight this region strongly, such as the Stark potential Fz, or any operator of the form $r^j, j \geq 0$, can be reliably evaluated from such wave functions. This approach underlies the Bates-Damagaard method, which has been widely employed in calculations of oscillator strengths for the lower states of the alkali metals.[6] Rydberg states are particularly well suited to the Coulomb approximation since Rydberg electrons are localized far from the core. Another important consideration to our approach is that off-diagonal matrix elements for operators of the form $r^j, j \geq 0$, decrease rapidly as the energy difference between the states increases. Thus eigenvalues and eigenvectors in a particular energy region can be obtained by diagonalizing the energy matrix including only those states which are local in energy. It is, of course, essential to confirm the accuracy of the method. We shall do this by checking our calculated results for hydrogen with the predictions of perturbation theory and also by comparing the results for several alkali metals with experiment.

At first glance the zero-field parabolic representation provides an attractive basis for the Stark problem because it is partially diagonal. Unfortunately, employing the Coulomb approximation with a parabolic representation presents practical difficulties. The unperturbed energies for the alkali metals are diagonal in a spherical, not a parabolic, basis. Thus one must not only transform between parabolic and spherical representations,[7] but also generalize the parabolic states to

nonintegral order. A more fundamental problem is that the Stark effect for the alkali metals is not diagonal in the parabolic basis, so that most of the advantage is lost.

Because of these difficulties we have chosen to work with a spherical representation. The matrix elements of the Stark interaction have the form

$$\langle W,l,m|Fz|W',l',m'\rangle = \delta_{m,m'}\delta_{l,l'\pm1}F\langle l,m|\cos\theta|l'm'\rangle \times\langle W,l|r|W',l'\rangle. \tag{8}$$

The angular matrix elements are derived using elementary algebra of spherical harmonics, which gives the familiar result

$$\langle l,m|\cos\theta|l-1,m\rangle=\left(\frac{l^2-m^2}{(2l+1)(2l-1)}\right)^{1/2},$$
$$\langle l,m|\cos\theta|l+1,m\rangle=\left(\frac{(l+1)^2-m^2}{(2l+3)(2l+1)}\right)^{1/2}. \tag{9}$$

The principal computational task is to evaluate the radial-matrix elements efficiently and accurately. Numerous analytic formulas have been proposed, but we have found that numerical integration of the radial equation is most satisfactory. The method has advantages of speed and accuracy and also permits inclusion of perturbations to the Coulomb potential, such as the r^{-3} fine structure interaction or the r^{-4} core-polarization term. The method is described in Appendix A.

B. Region of study

The decision to calculate the Stark structure in the vicinity of $n=15$ was prompted by several considerations. The mean density of Rydberg Stark states for a fixed value of $|m|$ scales as n^4; for $n=15$ the average spacing between levels is 3 cm^{-1}, well suited to our experimental resolution of 0.2 cm^{-1}. Also, we desired to display the Stark structure graphically so that qualitative features could be easily identified. In the region of $n=15$ the plots are simple enough for the entire structure to be discernible in a single map; for higher values of n the situation becomes so complex that local regions of the Stark map would have to be displayed separately. Lastly, for a given precision the size of the required basis set scales as n^2. The basis needed for $n=15$ matched the capacity of the minicomputer with which the calculations were carried out (64 k bytes of memory).

The maximum electric field was taken to be 6 kV/cm. This is the approximate "threshold" field for ionization in the region studied. Although well defined levels exist above the threshold field,[4] the situation in that region can become complicated due to damping effects, and the Stark structure calculations must be modified.

C. Fine structure

For the heavy alkali metals the fine-structure interaction is large enough to influence the Stark structure and must be taken into account. With a spherical basis this is straightforward. The total angular momentum is $j=l\pm\frac{1}{2}$, and the Stark interaction has matrix elements

$$\langle W,l,j,m_j|Fz|W',l',j',m_j'\rangle = \delta(m_j,m_j')\,\delta(l,l'\pm1)\langle W,l|r|W',l'\rangle F \times\sum_{m_l=m_j\pm\frac{1}{2}}\langle l,\tfrac{1}{2},m_l,m_j-m_l|j,m_j\rangle\langle l',\tfrac{1}{2},m_l,m_j-m_l|j,m_j\rangle\langle l,m_l|\cos\theta|l',m_l\rangle. \tag{10}$$

The first two factors in the sum are Clebsch-Gordan coefficients. The angular-matrix element is given by Eq. (9). Note that the radial-matrix element is calculated using the exact energy of the state, including fine structure.

Taking fine structure into account doubles the basis set; for each value of m_j we must include the two values $m_l=m_j\pm\frac{1}{2}$. The problem can be avoided for the lighter alkali metals by treating fine structure as a perturbation after the diagonalization is completed. The diagonalizations must be done twice, however, once for each of the two values of m_l. The energies of the basis states are taken to be at the "center of gravity" of the fine-structure multiplets. If the fine-structure interaction $\xi\vec{L}\cdot\vec{S}$ is small compared to the term separation, the $\vec{L}\cdot\vec{S}$ matrix elements which are diagonal in n, $\xi_{n,n}$ are known accurately from the zero-field fine-structure energy splittings. The fine-structure interaction depends on the behavior of the wave functions near the origin. For a given value of l this varies only with normalization. Consequently, the off-diagonal elements can be estimated accurately from

$$\xi_{n,n'} = (\xi_{n,n}\xi_{n',n'})^{1/2}. \tag{11}$$

It should be noted that the fine-structure (fs) operator can itself be modified by the applied electric field. We can write the operator as

$$\begin{aligned}\mathcal{H}_{\rm fs} &= \tfrac{1}{2}\alpha^2(\vec{E}\times\vec{p})\cdot\vec{S}\\ &= \tfrac{1}{2}\alpha^2[(-\vec{\nabla}V + F\hat{z})\times\vec{p}]\cdot\vec{S}\\ &= \tfrac{1}{2}\alpha^2\frac{1}{r^3}\vec{L}\cdot\vec{S} - \tfrac{1}{4}i\alpha^2F(p_-S_+ - p_+S_-),\end{aligned} \tag{12}$$

where $p_\pm = p_x \pm ip_y$. The field-dependent term leads to the selection rules $\Delta l = \pm 1$, $\Delta m_l = \pm 1$, and $\Delta m_j = 0$. Comparing the two terms at the ionization field $F \approx 0.1/n^4$ yields

$$\frac{W_{\rm fs}(\rm elec)}{W_{\rm fs}(\rm normal)} = \simeq \frac{F\langle p\rangle}{l\langle r^{-3}\rangle} \simeq \frac{0.1}{n^4}\frac{\langle r^{-1}\rangle}{\langle r^{-3}\rangle} \simeq 0.1\frac{l^3}{n^3}, \tag{13}$$

which is small except for states with $m_j \approx n$. Physically, parabolic wave functions which are concentrated near the potential maximum experience a total electric field which is weak and consequently have a small fine-structure interaction. Thus it is expected that states whose energy decreases with increasing field will have a slightly depressed fine-structure interaction while states with increasing energy will have a slightly enhanced fine-structure interaction.

The results presented in Sec. VI were treated for fine structure according to Eq. (10). Fine structure was taken into account for rubidium and cesium only, since the splittings were unresolvable on the Stark maps for the lighter alkali metals.

D. Oscillator strengths for excitation of a stark manifold

For some purposes it is desirable to calculate the intensity of excitation of Stark states from a low-lying state. The oscillator strength for a transition from a ground state W, l, m to a Stark state W', m' is

$$f_{W,W'} = \tfrac{2}{3}(W - W')\left|\sum_{W''}\sum_{l''} U^{W'}_{W'',l''}(F) \times \langle Wlm|\hat{\epsilon}\cdot\vec{r}|W''l''m'\rangle\right|^2, \tag{14}$$

where $U^{W'}_{W'',l''}(F)$ is the unitary transformation which diagonalizes the Stark matrix. Although the Coulombic approximation is not well suited to calculating accurate matrix elements involving low-lying states, it can yield accurate relative values for matrix elements from a given low-lying state to various Rydberg states. Thus the distribution of oscillator strengths among a manifold of Rydberg Stark states should be given reliably by Eq. (14).

IV. ACCURACY AND SOURCES OF ERROR

In this section we discuss the accuracy of our calculations and the various sources of error. Because atomic units are not particularly well suited for examining errors we shall quote the errors in spectroscopic units, $\rm cm^{-1}$. The following magnitudes for $n = 15$, hydrogen, may be helpful in judging their relative significance: (a) The term separation is 65 $\rm cm^{-1}$, (b) the first-order separation between Stark subcomponents at 6 kV/cm is 11 $\rm cm^{-1}$, and (c) the maximum fourth-order Stark effect at 6 kV/cm is 0.07 $\rm cm^{-1}$.

The goal of accuracy in these calculations is 0.05 $\rm cm^{-1}$, though in many regions the maps of the Stark structure are considerably more accurate than this. The numerical errors are generally determined by comparing calculations for hydrogen with the results of perturbation theory evaluated through fourth order.

A. Effects due to the truncated basis set

Our treatment becomes progressively less accurate as the electric field increases because the errors generally grow with the size of the perturbation for approximation methods based on expansion in a truncated set of basis states. Truncation errors grow rapidly with the field and tend to be greatest for the extreme Stark components of a given term. This trend is shown in Table I, which displays the energy errors for various Stark sublevels of $m = 0$ states for $n = 15$ at 3 and 6 kV/cm, for various sizes of basis sets. (The parabolic number n_1 has the value of 14, 7, and 0 for the highest, intermediate, and lowest Stark sublevels, respectively.) Table I reveals that the basis set $n = 13$–20 is essentially adequate to provide an accuracy of 0.05 $\rm cm^{-1}$. The maximum error occurs for the outermost Stark components at the largest field. (At 6 kV/cm the errors actually exceeds 0.05 $\rm cm^{-1}$ for the $n_1 = 0$ state, but this level is so close to the ionization limit that our treatment

TABLE I. Energy error (in $\rm cm^{-1}$) of several $n = 15$, $m = 0$ Stark levels. Positive error indicates that the calculated energy is too high.

		Terms included in basis set			
Field	n_1	$n=15$	14–16	13–18	13–20
3 kV/cm	14	0.70	0.25	0.01	−0.02
3 kV/cm	7	0.91	0.11	0.00	0.00
3 kV/cm	0	0.83	−0.03	0.00	0.00
6 kV/cm	14	2.73	1.59	0.23	0.04
6 kV/cm	7	3.70	0.92	0.03	0.00
6 kV/cm	0	3.59	−0.41	0.13	0.08

cannot be used with confidence. At 5 kV/cm the error is less than 0.03 cm^{-1} and below 4 kV/cm it is less than 0.01 cm^{-1}.)

B. Effects of errors in the matrix element

Various errors can affect the precision of the matrix elements, and these all represent potential sources of error in the Stark energies. It is difficult to predict generally how the error in a given matrix element propagates, but it is possible to place a limit on the resulting errors in the eigenenergies. If *all* the matrix elements are in error by the same fractional amount, the result is equivalent to a rescaling of the electric field. The maximum first-order Stark shift of the term $n=15$ at 6 kV/cm is 40 cm^{-1}; if we take 0.04 cm^{-1} as the maximum tolerable energy error, then the matrix elements must be reliable to 0.01%. A more realistic situation, however, is one in which the matrix-element errors are largely uncorrelated and their effects largely cancel. If the errors arise from only a few of the matrix elements, their effect is generally diluted due to the strong mixing of the spherical states.

C. Sources of error in the matrix elements

As discussed in Appendix A, numerical integration of Schrödinger's equation leads to matrix-element errors which are generally less than 0.001%, so that for our purposes the integration procedure is essentially exact. Nevertheless, errors in the matrix elements can arise from approximations required to treat the core and from corrections for other non-Coulombic effects. Deviations from pure Coulombic behavior for single-electron systems divide naturally into short-range and long-range effects. The short-range effects arise from the tightly bound inner-core electrons which cause departures from a $-1/r$ potential. The long-range effects are due to core polarization and fine structure.[8]

1. Normalization error

The major effect of the core is to shift the energy of the penetrating (low l) states. These shifts are well described by quantum-defect theory. The quantum defects are frequently known from spectroscopic studies and are essentially treated as empirical constants in generating the Coulombic wave functions. Although these wave functions are accurate outside the core where the major contributions to the matrix elements arise, there is a small uncertainty in the normalization of the wave functions due to their unknown shapes at short range. This uncertainty is the leading error due to the core. The simplest way to treat the normalization problem is to terminate the wave functions near the core and neglect their short-range contributions to the matrix elements. Because the density of wave function near the origin varies as $1/n^3$, the error decreases rapidly with n. As we shall show, even in the worst case this cutoff procedure introduces negligible error for $n=15$ states.

To put an upper limit on the normalization error we have compared matrix elements with various radii for the inner cutoff with exact results for hydrogen. (The actual errors for the alkali metals will be substantially less because the high kinetic energy of the electron within the core decreases the amplitude there.) In calculating the alkali-metal matrix elements, the cutoff radius was taken to be the effective core radius $\alpha_d^{1/3}$, where α_d is the dipole polarizability of the core. For the alkali metals, α_d ranges from 0.2 to 20 a.u. Table II shows results for matrix elements between a variety of states in the $n=15$ region. As expected, the normalization error is only observable for low-l matrix elements. In the worst case, an s-p transition with $\alpha_d=100$, the error is less than 0.1%.

2. Errors due to long-range deviations from the Coulomb potential

Outside the core, deviations from the Coulomb potential arise from core polarization and fine structure. Core polarization results in a perturbation with a leading term[8]

$$V_p=-\tfrac{1}{2}\alpha_d\,1/r^4\,, \tag{15}$$

where α_d is the dipole core polarizability. The fine-structure interaction is

TABLE II. Fractional change in dipole-matrix elements due to cutoff at core and to core polarization potential.

States	α_d	(a)	(b)
15,0; 15,1	10	1.3×10^{-4}	1.7×10^{-4}
	100	5.9×10^{-4}	6.7×10^{-4}
	1000	1.7×10^{-3}	1.9×10^{-3}
15,6; 15,7	10		3.0×10^{-5}
	100		2.5×10^{-4}
	1000		1.9×10^{-3}
15,13; 15,14	10		3.3×10^{-5}
	100		3.1×10^{-4}
	1000		2.8×10^{-3}
15,0; 18,1	10	1.1×10^{-4}	1.7×10^{-4}
	100	5.7×10^{-4}	6.9×10^{-4}
	1000	1.8×10^{-3}	2.3×10^{-3}

[a] Fractional error for inner radial cutoff at $r=\alpha_d^{1/3}$.
[b] Fractional error for column (a) plus effect of polarization potential.

$$V_{fs} = \tfrac{1}{2}\alpha^2(1/r^3)\vec{L}\cdot\vec{S}, \tag{16}$$

where α is the fine-structure constant. As Table II shows, including V_p in the potential produces small though observable corrections. No shift in the matrix elements occur due to V_{fs} at a level of precision of 1 part in 10^5. Because inclusion of V_p and V_{fs} introduces such minor corrections to the electric field matrix elements, they have been dropped and the potential taken to be exactly $1/r$.

D. Quantum defects

A Coulombic state is specified by its energy and angular momentum. The term energies of the alkalis are most commonly expressed in the form

$$W(n, l) = -\tfrac{1}{2}(n^*)^{-2}, \tag{17}$$

where $n^* = n - \delta_l$, and the quantum defect δ_l is a constant, or a slowly varying function of energy, for each value of l. Thus the quantum defects provide a complete specification of the structure and behavior of a Rydberg system. Errors in them lead inevitably to errors in the Stark structure.

It is useful to regard a quantum defect as a measure of the departure of an energy level from the hydrogenic value.

$$\Delta W(\delta) = -\frac{1}{2}\left(\frac{1}{(n^*)^2} - \frac{1}{n^2}\right) \cong -\frac{\delta}{n^3}; \tag{18}$$

if we compare this result with the term separation $\Delta W_0 = -1/n^3$ [Eq. (4)], we see that

$$\Delta W(\delta) = \delta \Delta W_0. \tag{19}$$

Thus if the energy is to be known to within 1% of the term separation, δ must be known to 1%. More precisely, the nonintegral portion of δ must be known to 0.01.

Errors in the quantum defects enter the Stark structure in two ways: through errors in the zero-field eigenenergies and through errors in the matrix elements. The first error is generally not serious for the observed energies can always be used to correct the quantum defects to the accuracy needed. Thus for $n = 15$, where $\Delta W_0 = 40$ cm^{-1}, spectroscopic measurements at zero field within an accuracy of 0.04 cm^{-1} directly yield quantum defects within an accuracy of 0.1%. Often this accuracy is not actually needed. If the Stark interaction is large compared to $\Delta W(\delta)$, which is usually the case except at very low fields, the levels are so strongly mixed that the errors in the quantum defects are averaged throughout the Stark manifold, reducing their effect on any single level. (The level structure at level anticrossings is highly sensitive to the quantum defects, however, and small errors may have conspicuous effects. We shall consider the role of quantum defects at anticrossings in Sec. VII.)

Let us turn to the effect of quantum defects on the matrix elements. If the quantum defect for a particular state is in error, all the matrix elements involving that state will be affected. The final errors in the Stark energies will vary with the size of the quantum defect. Figure 1 shows $\langle n^*, 1|r|15, 0\rangle$, the s-p matrix elements from the 15s state to the n^*p state, where n^* ranges from 14 to 23. The matrix element varies most rapidly near $n^* = 15.8$, or $\delta = 0.2$. From Fig. 1 we can find a limit on the tolerable error in δ. If the energy is to be precise within 0.05 cm^{-1} at 6 kV/cm, the matrix elements must be accurate to within 0.2 a.u. A change in δ of 0.25 yields a change in the matrix element of 100 a.u. Thus for a precision of 0.2 a.u., δ must be known to ± 0.0005. This represents a limit to the average error for all the quantum defects and, because the defects are uncertain only for the lowest angular-momentum states, errors a good deal larger are often tolerable. Thus errors in the matrix elements due to uncertainties in the quantum defects are generally not important.

V. EXPERIMENTAL PROCEDURE

In order to assure that our calculations are realistic and to check their accuracy, we have measured experimentally the Stark structure of two alkali metals, lithium and cesium. We selected these for comparison with our calculations because lithium and cesium are respectively the most hydrogenlike and the least hydrogenlike alkali metals and because they represent extreme cases in which fine structure may and may not be ignored.

Excitation spectra were obtained at numerous

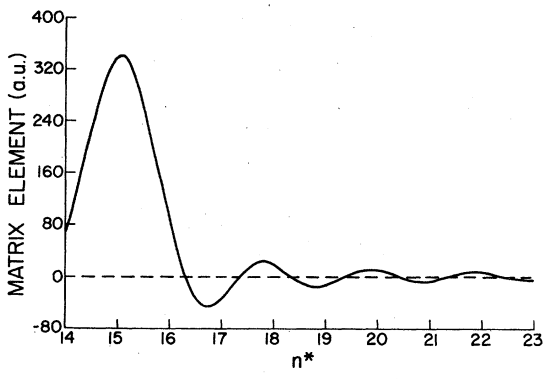

FIG. 1. Variation of the radial-matrix element $\langle n^*, 1|r|15, 0\rangle$ with effective quantum number n^*.

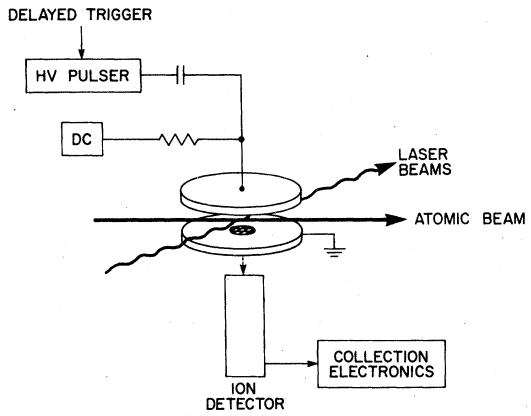

FIG. 2. Experimental arrangement.

values of an applied electric field in the energy region about $n=15$. At each field, atoms in a beam were excited stepwise from the ground state via resonant intermediate states. The Stark structure was displayed by sweeping the final laser while monitoring the excited-state population by the technique of pulsed-field ionization.[9] A schematic diagram of the experimental arrangement for lithium is shown in Fig. 2. An effusive beam provided a density of 10^9 atoms/cm^3 at the interaction region with a mean atomic speed of 1 mm/μsec. The interaction region was defined by the intersection of the atomic beam with the three laser beams. The first laser was tuned to the transition $2s \rightarrow 2p$ (671 nm) and the second was tuned to the transition $2p \rightarrow 3s$ (813 nm). The final laser was swept over a 100-cm^{-1} interval centered on the $3s \rightarrow 15p$ transition (626 nm); its polarization was adjusted to be parallel or perpendicular to the field to excite states with $|m|=0$ or 1, respectively.

The pulses from the first two lasers were simultaneous and the final pulse was delayed until the initial pulses were extinguished, about 5 nsec. The lasers were all of the "grazing-incidence" type[10] with a peak power of 2 kW and a linewidth of 0.2 cm^{-1}. All three lasers were pumped by harmonics of a Nd:YAG laser.

The interaction region was centered between two electric field plates separated by 0.500(5) cm. The static field was applied by a well regulated high-voltage supply. Atoms in Rydberg states were detected by applying a 10 kV/cm field about 3 μsec following excitation. This pulsed field ionized all Rydberg atoms present and accelerated the ions toward a grid-covered hole in the grounded electric field plate. The ions were detected by an electron multiplier. The multiplier output was measured with a gated integrator and the data were stored and processed for display by a laboratory computer.

The measurements of cesium employed a similar procedure, except for the excitation scheme. The first laser was tuned to the transition $6s \rightarrow 7p$ (455 nm). The atoms were allowed to decay radiatively to the $7s$ level and 40 nsec following the first laser pulse a second laser at 810 nm excited transitions from the $7s$ level to the Rydberg states. The second laser was linearly polarized parallel to the electric field so that only $|m_j|=\frac{1}{2}$ states were excited.

The electric field was known absolutely to about 2% and was calibrated to within 1% by careful mapping of a level crossing. The two methods gave good agreement. Nonlinearities in the laser scans for lithium presented a somewhat more troublesome error. Discrepancies up to 0.5 cm^{-1} occurred in the first 15% of the laser scan (540–525 cm^{-1}), but the discrepancies for the $|m|=1$ and $m=0$ data were so well correlated that the source of the error was unambiguous.

VI. STARK STRUCTURE OF ALKALI METALS

In this section we present our calculations of the Stark structure of the alkali metals and our experimental data for lithium and cesium. The results are displayed as a series of maps. In two cases, lithium and cesium, the calculated energy levels are compared with experimental data. We have worked in a single range of energy and electric field: 440–540 cm^{-1} and 0–6 kV/cm, respectively. These values encompass the $n=15$ manifold at fields up to the ionization region.

The energies were calculated at 100 V/cm intervals and the energy-level plots were generated by connecting the eigenvalues, using quadratic interpolation between the field points. It is important to realize that Stark-structure plots based on calculations at a finite grid of field values will display spurious level anticrossings if the field values happen to straddle a level crossing. The maximum size of the apparent level repulsion at such a spurious anticrossing is approximately $\frac{1}{2}(dW/dF)\Delta F$, where dW/dF is the relative slope of the levels and ΔF is the electric field grid interval. Such errors are generally less than 1 cm^{-1}, but they can be discerned in certain plots. For instance, all the anticrossings visible in the $|m|=1$ Stark map for lithium (Fig. 3) are due to this cause. Thus level repulsions greater than 1 cm^{-1} are real, but smaller ones may be artifacts of the plotting procedure. In order to study an anticrossing in detail the energies must be calculated at several values of the field in the immediate vicinity of the anticrossing. An example of this procedure is displayed in Sec. VII.

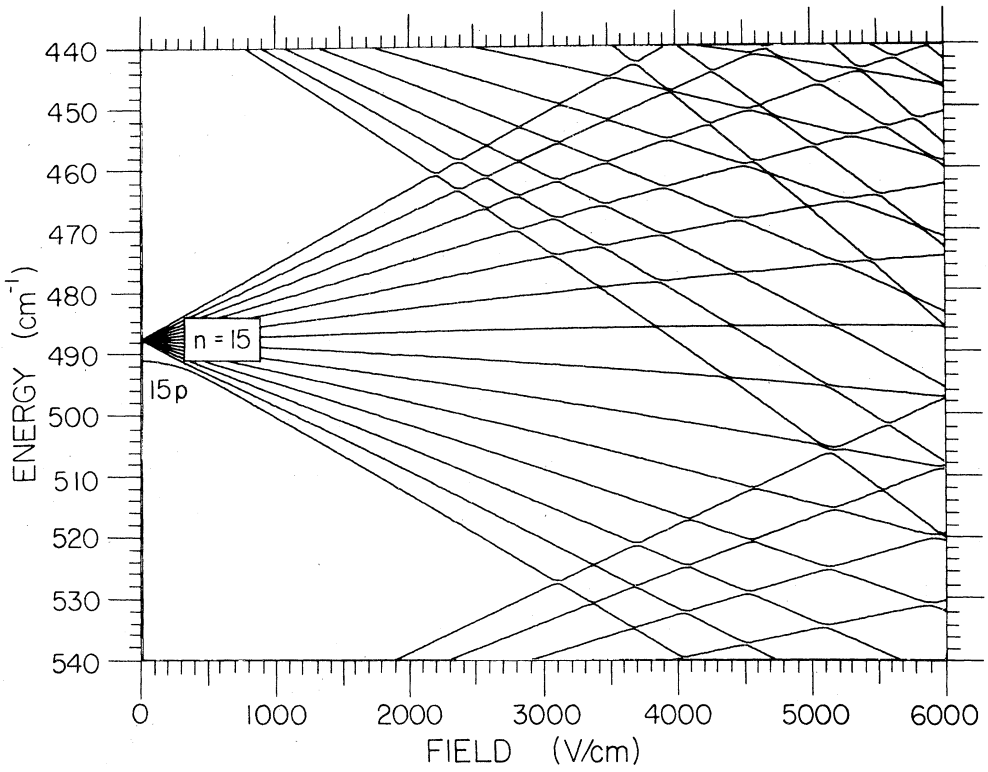

FIG. 3. Lithium, $|m|=1$.

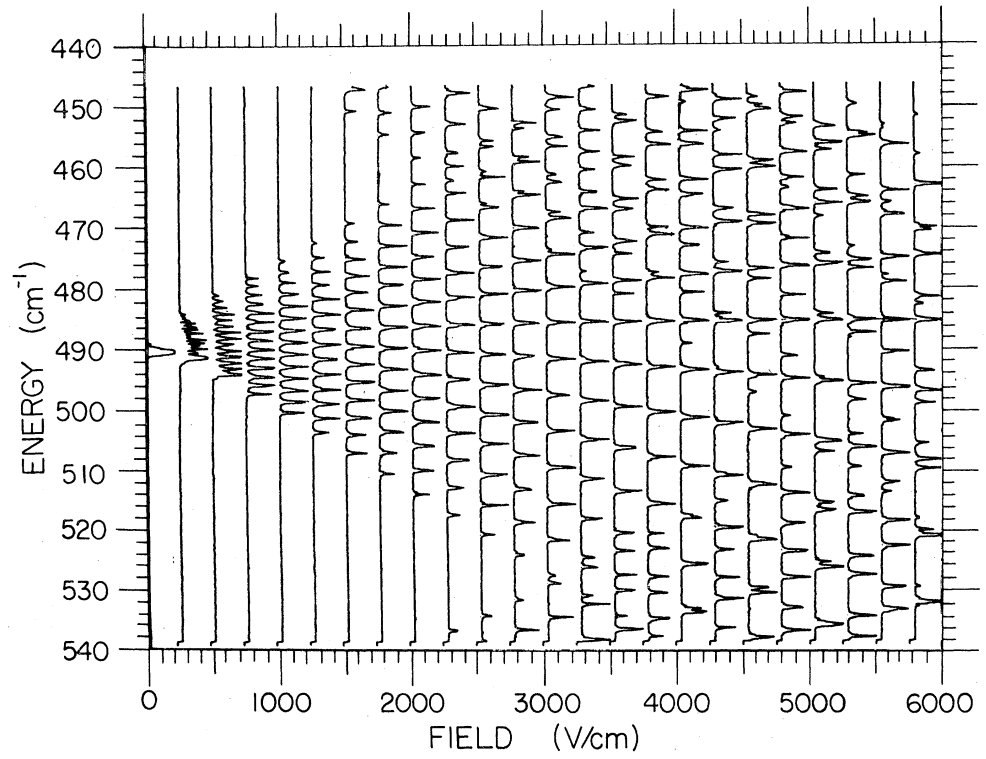

FIG. 4. Lithium, $|m|=1$; experimental Stark structure.

TABLE III. Quantum defects of the alkali metals.

Atom	l	δ_l	Levels [a]	Ref.	Atom	l	j	δ_j	Levels [a]	Ref.
Li	0	0.399(6)	10,11	11	Rb	0	$\frac{1}{2}$	3.135(1)	10 → 12	11
	1	0.053(9)	10 → 20	11		1	$\frac{1}{2}$	2.658(1)	10 → 20	11
	2	0.002	12	11		1	$\frac{3}{2}$	2.645(1)	10 → 20	11
Na	0	1.3470(14)	23 → 41	12		2	$\frac{3}{2}$	1.343(2)	10 → 13	11
	1	0.8541(13)	23 → 41	12		2	$\frac{5}{2}$	1.341(2)	10 → 13	11
	2	0.0144(4)	23 → 41	12	Cs	0	$\frac{1}{2}$	4.057(2)	11 → 12	11,14
K	0	2.178(6)	10 → 20	13		1	$\frac{1}{2}$	3.595(3)	10 → 20	11
	1	1.712(2)	10 → 17	13		1	$\frac{3}{2}$	3.562(3)	10 → 20	11
	2	0.267(1)	10,11	13		2	$\frac{3}{2}$	2.476(0)	10 → 20	11,15
	3	0.010(1)	10 → 14	13		2	$\frac{5}{2}$	2.467(0)	10 → 20	11,15
						3	$\frac{5}{2}$	0.033(1)	10 → 12	14
						3	$\frac{7}{2}$	0.033(1)	10 → 12	14

[a] Principal quantum numbers of terms observed.

The quantum defects and core polarizability used in the calculations are listed in Tables III and IV, respectively.[11-16] The quantum defects were derived from the most authoritative spectroscopic data that we have been able to obtain, though effects of errors less than about 0.01 are not actually visible in the maps.

A. Lithium

Turning first to the results for $|m|=1$, Fig. 3, we observe the typical hydrogenlike behavior of a system with small quantum defects. The only noticeable departure from pure hydrogenic behavior is the depression of the p state visible at zero field. Because of its nonvanishing quantum defect ($\delta_1 = 0.05$), the p state initially experiences a second-order Stark effect, in contrast to the first-order behavior of the remaining levels. If the field exceeds about 400 V/cm, however, the p state merges into the "fan" of linear states and the Stark map becomes indistinguishable from a map for hydrogen. At about 2.1 kV/cm the uppermost level of the $n=15$ manifold encounters the lowest level of the $n=16$ manifold and at 3.1 kV/cm the first encounter with an $n=14$ level occurs. As explained previously, the anticrossings which are observable between numerous levels are actually artifacts of the plotting procedure; the true level repulsions are too small to be observable.

TABLE IV. Dipole core polarizability of alkali metals.

Alkali metal	α_d (a.u.) [a]
Li	0.191
Na	0.945
	1.0015(15) [b]
K	5.490
Rb	9.023
Cs	14.752

[a] From Ref. 16.
[b] Experimental value from Ref. 8.

Experimental results for the $|m|=1$ states are displayed in Fig. 4, and in Fig. 5 they are shown superimposed on the calculated Stark map. The horizontal peaks represent the ion signal collected as the tunable laser passes through coincidence with a Stark state. The excitation curve for each scan has been plotted at its corresponding field value, so that the base of an excitation signal straddles the position of the true energy level. As expected, only the p state is excited at zero field (excitation is from the 3s level), though the entire Stark manifold is excited at even a small field. The intensity of the signals indicates that the p state is well distributed throughout the Stark manifold. The discrepancies in the positions of levels for the range 540–520 cm^{-1} are due to the nonlinearity of the laser drive.

The $m=0$ Stark maps, Figs. 6–8, provide a striking contrast to the case of $|m|=1$ and display many of the nonhydrogenic features typical of alkali-metal Stark structure. In the case of lithium these features arise entirely from a single large quantum defect, $\delta_0 = 0.35$. A conspicuous result is that the s levels never display linear Stark behav-

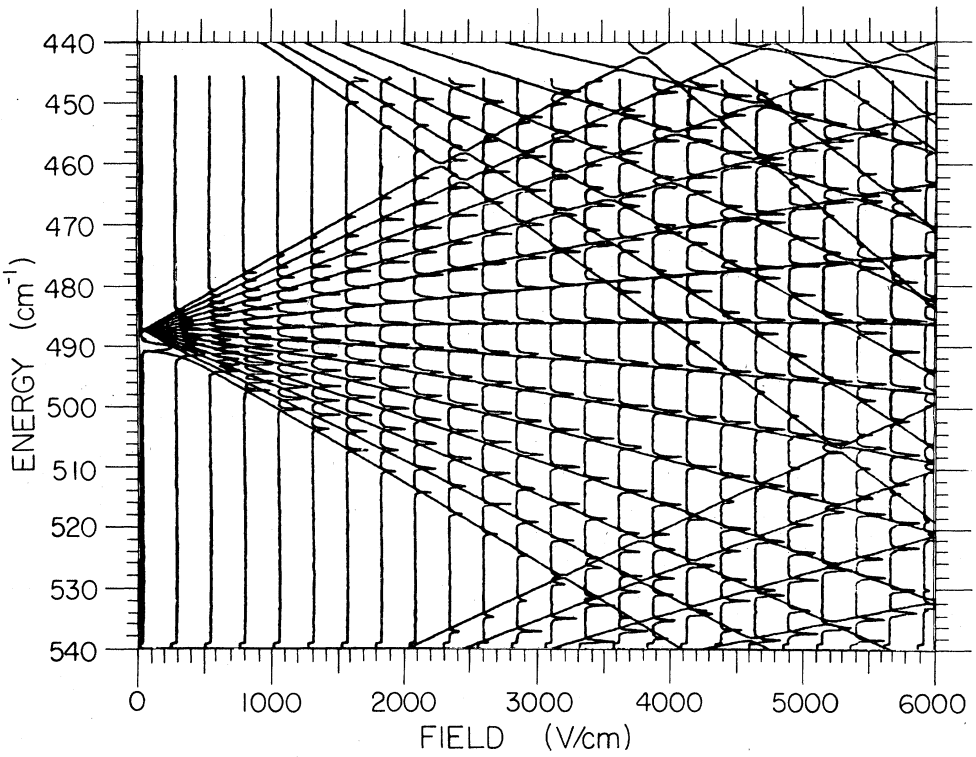

FIG. 5. Lithium, $|m|=1$; calculated and experimental Stark structure.

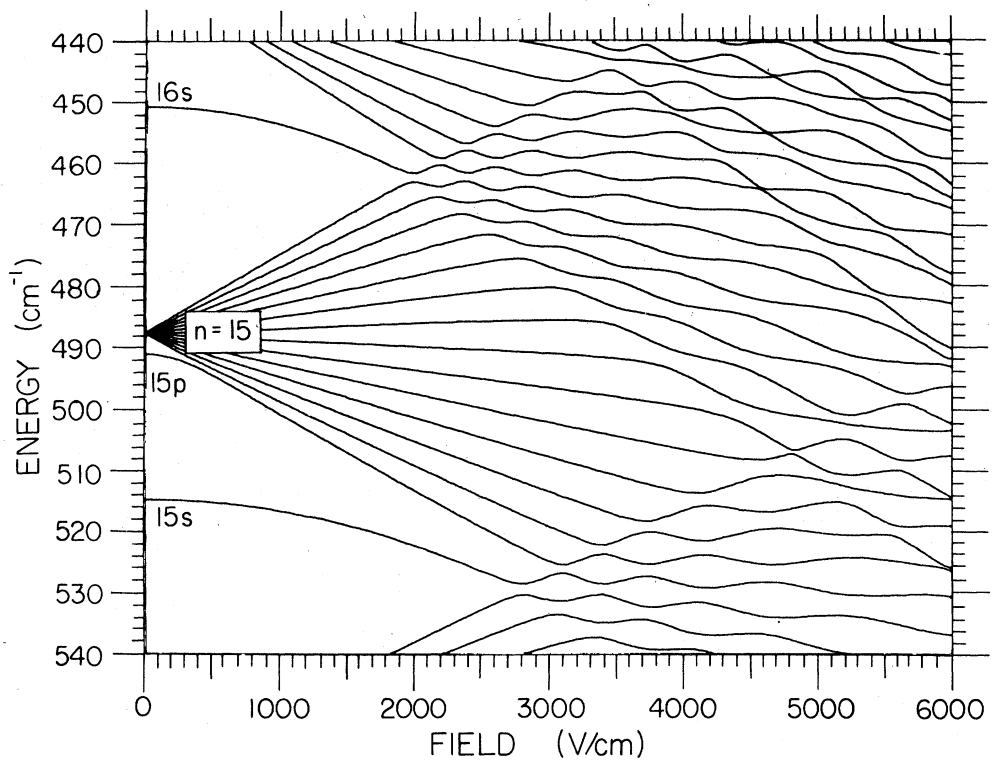

FIG. 6. Lithium, $m=0$.

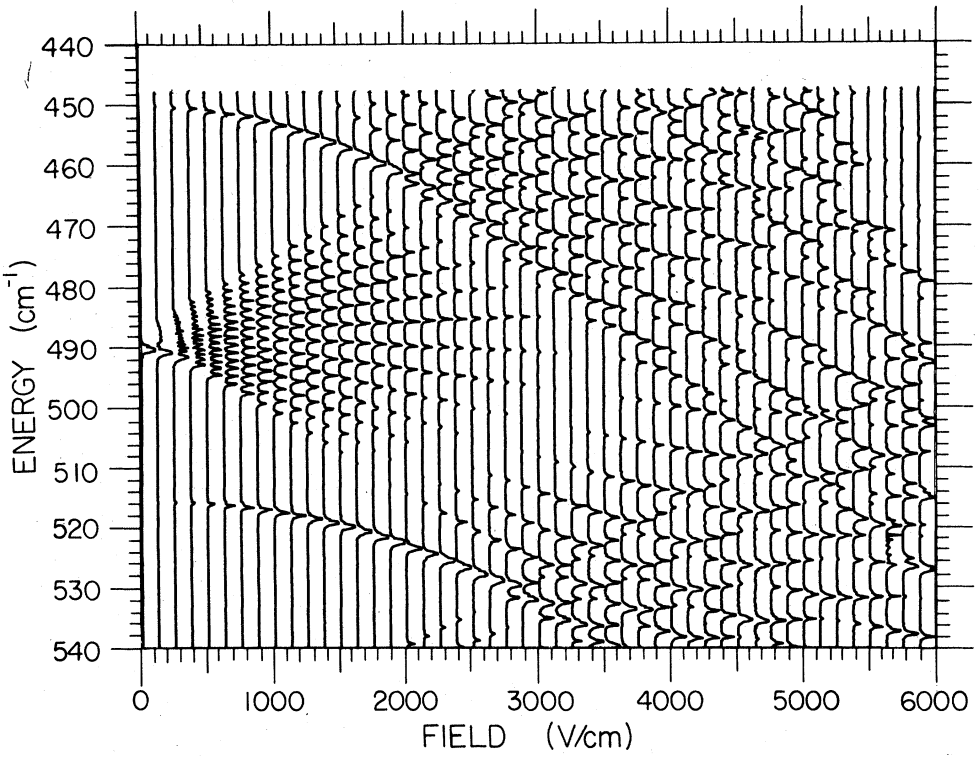

FIG. 7. Lithium, $m = 0$; experimental Stark structure.

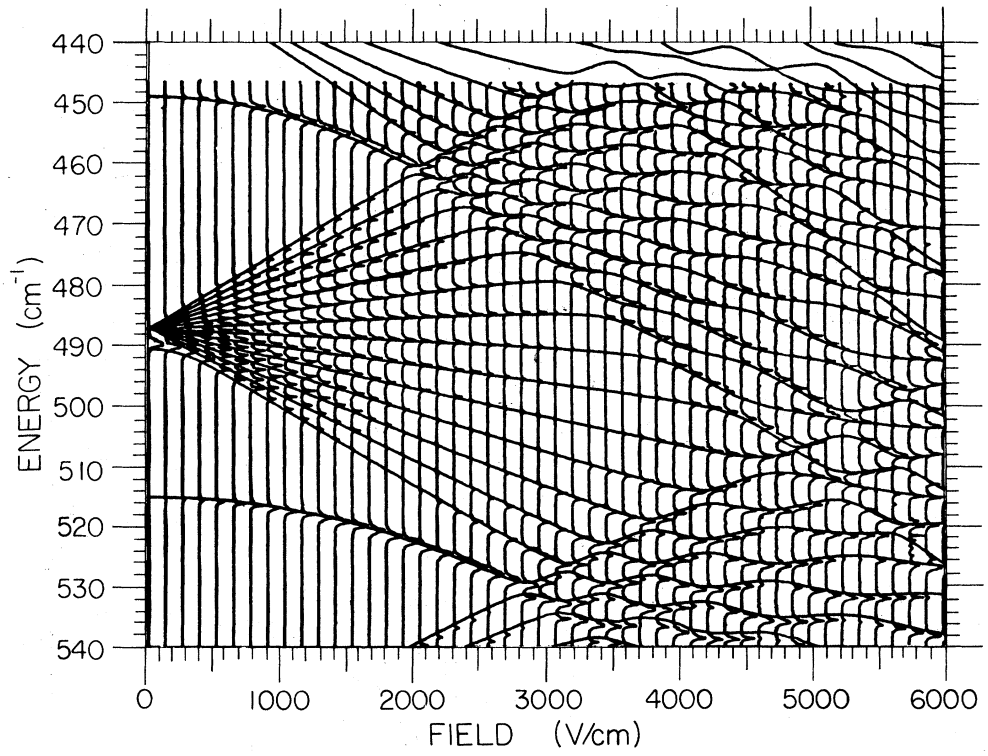

FIG. 8. Lithium, $m = 0$; calculated and experimental Stark structure.

ior. Instead they are repelled by levels above and below and are "squeezed" between the manifolds of the adjacent terms as the field increases. When this occurs the entire Stark structure becomes radically altered. The levels appear to interact strongly at high field and the resemblance to hydrogenic Stark structure is lost. This is in striking contrast to the $|m|=1$ behavior, Fig. 3, where the resemblance is preserved. Another notable feature is the appearance of regions where levels suddenly approach closely, or even appear to cross, for instance at 4.56 kV/cm, 455 and 465 cm^{-1} or 4.8 kV/cm and 507 cm^{-1}. As the data show (Figs. 7 and 8), such "crossings," or weak anticrossings, are quite real.

The line strengths for $m=0$ are qualitatively different from those for $|m|=1$. Large portions of the linear manifold disappear with increasing field, only to reappear at still higher fields. At the same time the s-state signal, absent at zero field, becomes extremely strong. These dramatic redistributions of oscillator strength provide an excellent opportunity for checking the calculated line intensities.

In Fig. 9 we display an expanded plot of a single laser sweep at 2.125 kV/cm. The most intense lines are clipped due to detector saturation, but the remaining lines are suitable for comparison with calculation. The relative line intensities shown on the data were calculated using the procedure described in Sec. III D. The oscillator-strength distribution in this region is extremely sensitive to the field and the best fit was obtained at a field 10 V/cm above the experimental value. (This adjustment is within the experimental uncertainty in the field.) Fluctuations in the pulsed lasers, combined with a relatively short averaging time, result in an uncertainty in the experimental line intensities of approximately 25%. Within this uncertainty the agreement with theory is good, particularly in view of the large variation in oscillator strength, greater than 30:1.

Sodium

Maps for the $|m|=1$ and $m=0$ Stark states of sodium are presented in Figs. 10 and 11, respectively. The $|m|=1$ map is similar to the $|m|=1$ map for lithium (Fig. 3) except that the nondegenerate p state now lies slightly above the linear manifold, rather than just below. [This state is actually a member of the term above, but because δ_1 is close to unity ($\delta_1=0.85$) each p level is effectively displaced downward one-term.] The "effective" quantum defect, $\delta_1-1=-0.15$, is large enough to induce sizable anticrossings, typically a few cm^{-1}. In contrast to Fig. 3, the anticrossings

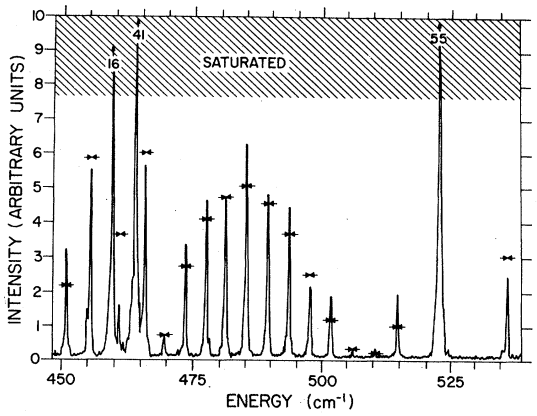

FIG. 9. Lithium, $m=0$; blowup of the scan at 2125 V/cm showing oscillator-strength distribution. Arrows indicate calculated distribution.

for sodium are quite real.

The $m=0$ Stark plot, Fig. 11, reveals an anomalously small second-order Stark effect for the s states. This occurs because the s states lie close to midway between the p states ($\delta_0-\delta_1=0.49$) and are repelled almost equally from above and below. Repulsions between the $m=0$ levels are so large that all character of the low-field states are lost at high fields and the energy levels generally slope downward. (Data displaying some of this behavior have been published previously.[17]) Nonetheless, apparent crossings can occur, as at 500 cm^{-1}, 4.5 kV/cm.

C. Potassium

The $|m|=2$ Stark structure of potassium, Fig. 12, is similar to the case of sodium $|m|=1$, (Fig. 10): A single nondegenerate level interacts with the linear manifold via a second-order Stark effect and finally joins the manifold. The $|m|=1$ and 0 states, however, have an anomalous Stark structure due to accidental coincidences among the quantum defects. These anomalies provide some useful insights on interactions among Stark states.

The p states of potassium lie practically midway between the d states because $\delta_1-\delta_2=0.54$. Consequently, the second-order Stark effect of the $|m|=1$ p states is extremely weak, as can be seen from Fig. 13. The p level effectively crosses into the linear manifold, showing no significant repulsion until very high fields. The reason is that the p state interacts only with the d-state component of the manifold, but the d component is small and second order at low fields.

A similar coincidence occurs for the $m=0$ levels (Fig. 14). The s state lies close to midway between the p states ($\delta_0-\delta_1=1.46$) and displays an extremely weak second-order Stark effect. Its inter-

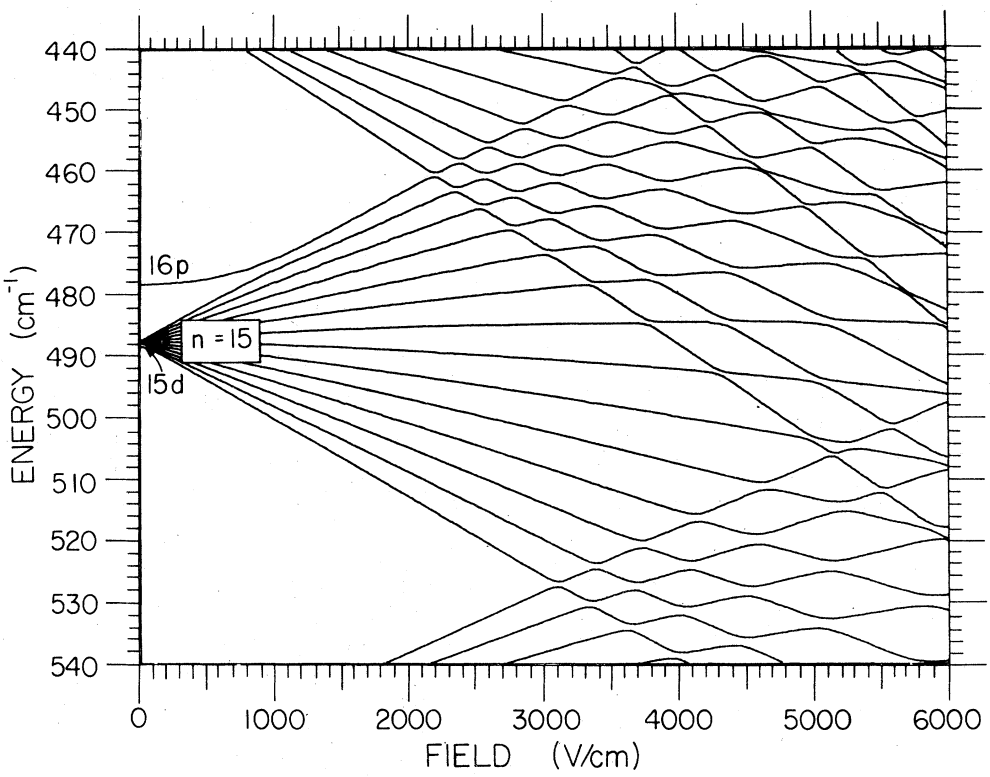

FIG. 10. Sodium, $|m|=1$.

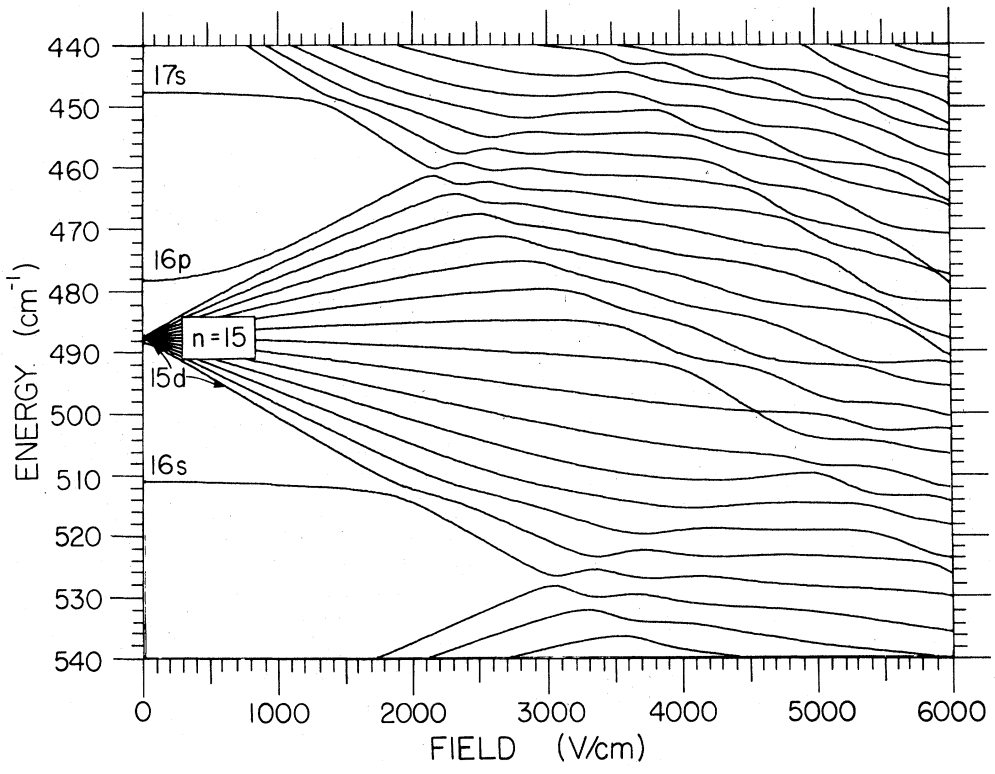

FIG. 11. Sodium, $m=0$.

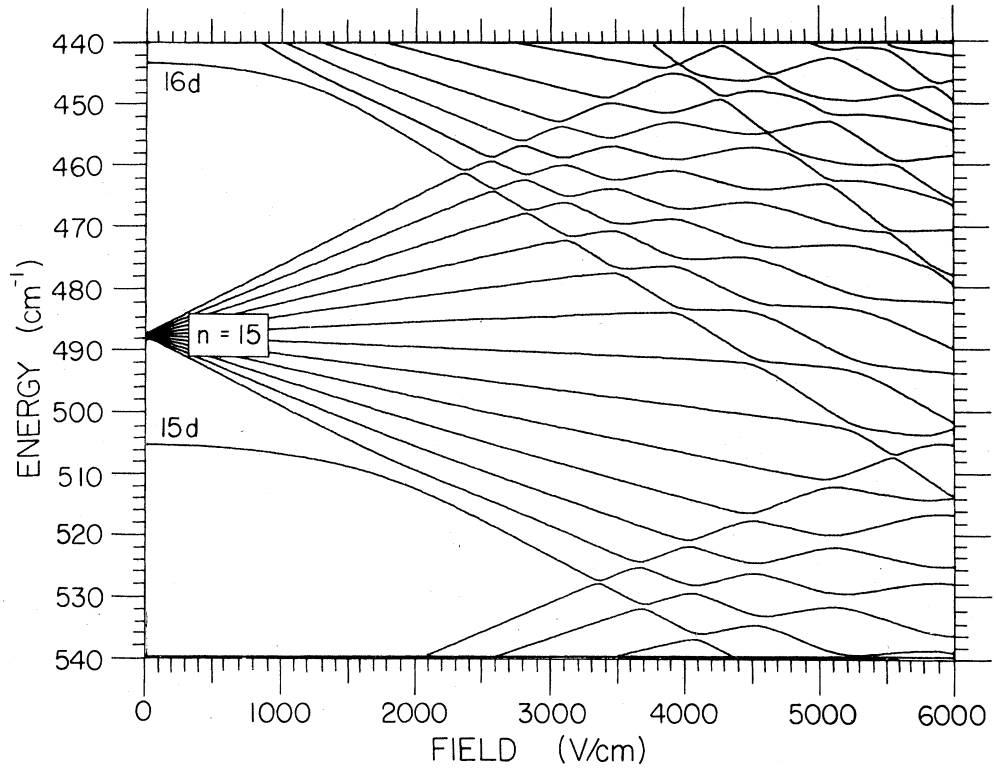

FIG. 12. Potassium, $|m|=2$.

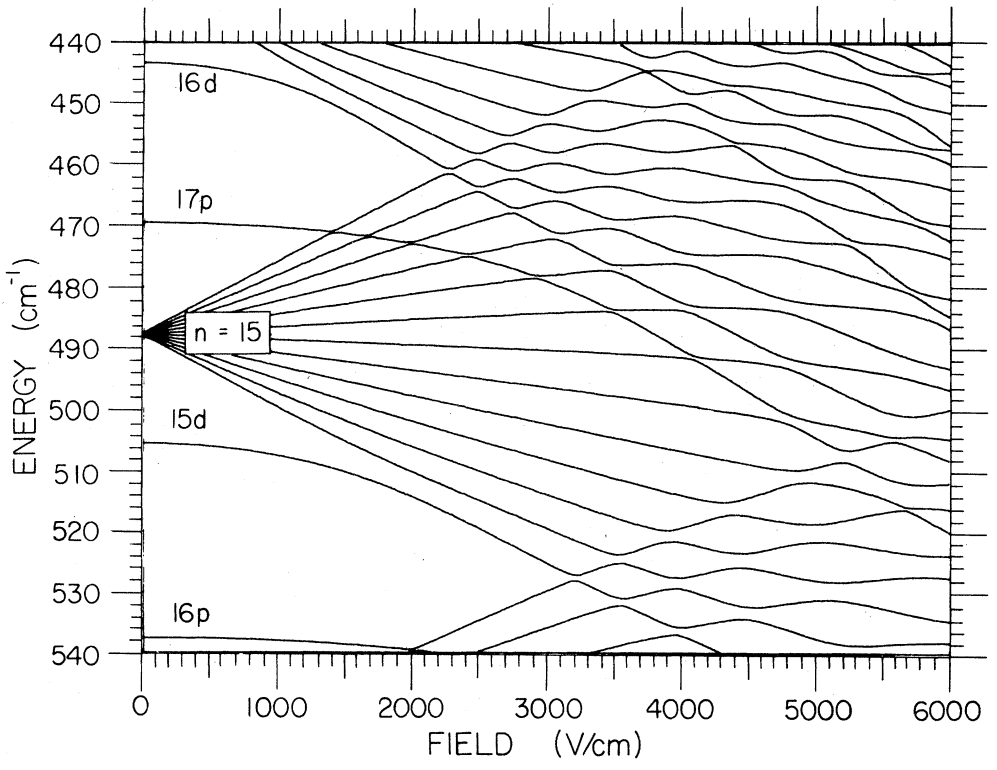

FIG. 13. Potassium, $|m|=1$.

action with the linear manifold, which depends on the p-state content, is third order, essentially negligible. For this reason the s state in Fig. 14 appears to be merely superimposed on the $|m|=1$ Stark map of Fig. 13.

D. Rubidium

The fine structure of the p and d states of rubidium is too large to be neglected, so that $|m_j|$ rather than $|m_l|$ is the "good" quantum number. Each $|m_j|$ manifold is a mixture of states with $m_l = m_j \pm \frac{1}{2}$. This effectively doubles the size of the basis set required for a given accuracy. Because our calculations were carried out with a fixed number of basis functions, the calculations are less accurate at high fields than those for the lighter alkali metals. Some discrepancies caused by this problem will be pointed out in the discussion of cesium.

The $|m_j|=\frac{5}{2}$ Stark map, Fig. 15, displays the characteristic effects of fine structure on Stark levels. At high fields two separate manifolds can be distinguished: the manifold of states $|m_l|=3$ and the manifold of states with $|m_l|=2$. The former is essentially hydrogenic, while the $|m_l|=2$ manifold shows the now familiar pattern of repulsions between Stark states in which a single level has a sizable quantum defect. The two manifolds interact via the fine structure of states with $l>2$, but this is so weak that they appear to cross.

The Stark map for $|m_j|=\frac{3}{2}$, Fig. 16, and $|m_j|=\frac{1}{2}$, Fig. 17, can be understood along similar lines, except that repulsions between the two manifolds now occur via the fine-structure interaction of the admixed low angular-momentum states. These are large enough to cause visible avoided crossings.

E. Cesium

The systematics of the cesium Stark structure are similar to those of rubidium and Figs. 18–20 are qualitatively similar to Figs. 15–17, respectively. Turning to the experimental Stark map for $|m_j|=\frac{1}{2}$, Fig. 21, and its comparison with theory, Fig. 22, systematic discrepancies can be observed in the upper right-hand quadrant. These errors are a result of effectively halving the basis set to accommodate the fine-structure effects. The calculated levels are generally too high, reflecting the omission of the higher n states which would depress the levels.

The oscillator strengths in Fig. 21 can be understood along the lines developed in the discussion of level mixing in potassium. The Rydberg states are populated from the $7S_{1/2}$ level and in zero field only the p state is excited. With increasing field the d levels become visible due to second-order mixing with the p state. The s states become visible at somewhat higher fields for the same reason. Finally, the p character mixes into the linear manifold via the d state, and the entire structure is displayed.

VII. LEVEL CROSSINGS AND ANTICROSSINGS

The regions of intersection between Stark levels of different terms are interesting theoretically and experimentally. The avoided crossings provide sensitive tests for Stark-structure calculations and can be studied in great detail since the relative positions of adjacent levels can be measured to a much higher precision than the positions of isolated levels. Furthermore, the systematics of pulsed field ionization frequently depend on nonadiabatic effects which occur as the states are swept through anticrossings in a rapidly rising field. Because the probability of a nonadiabatic transition depends exponentially on the level separations at the anticrossings, it is important to be able to calculate these separations accurately.

A. Level crossing in hydrogen

For hydrogen the Stark structure at the level intersections is unique. Nonrelativistic Stark levels cross in a pure Coulomb potential[5] but, as Hatton has pointed out,[18] inexact calculations of the Stark energies will generally predict spurious anticrossings. Thus the regions of level crossings for hydrogen are particularly suitable for testing the accuracy of our calculations.

We have calculated the separation at the first anticrossing between the $n=15$ and $n=16$ manifolds for various basis sets (see Table V). The states involved are $(15,14,0,0)$ and $(16,0,15,0)$, in the notation $(n,n_1,n_2,|m|)$. The apparent "repulsion" between these Stark levels was obtained by a careful mapping of the intersection region with a fine grid of field values. The error in the energy of the intersection varies between 0.75 and 0.002 cm^{-1}, depending on the basis set. Such errors are quite consistent with the expected calculational accuracy of individual levels in this region. The size of the separation between the levels, however, is surprisingly small; it varies between 2×10^{-4} and 5×10^{-4} cm^{-1} and is *least* for the *smallest* basis set. Apparently this separation reflects the residual numerical errors in the diagonalization procedure which grow with the size of the basis set, rather than errors resulting from an incomplete basis set. Thus we are assured that the level repulsions in alkalis pre-

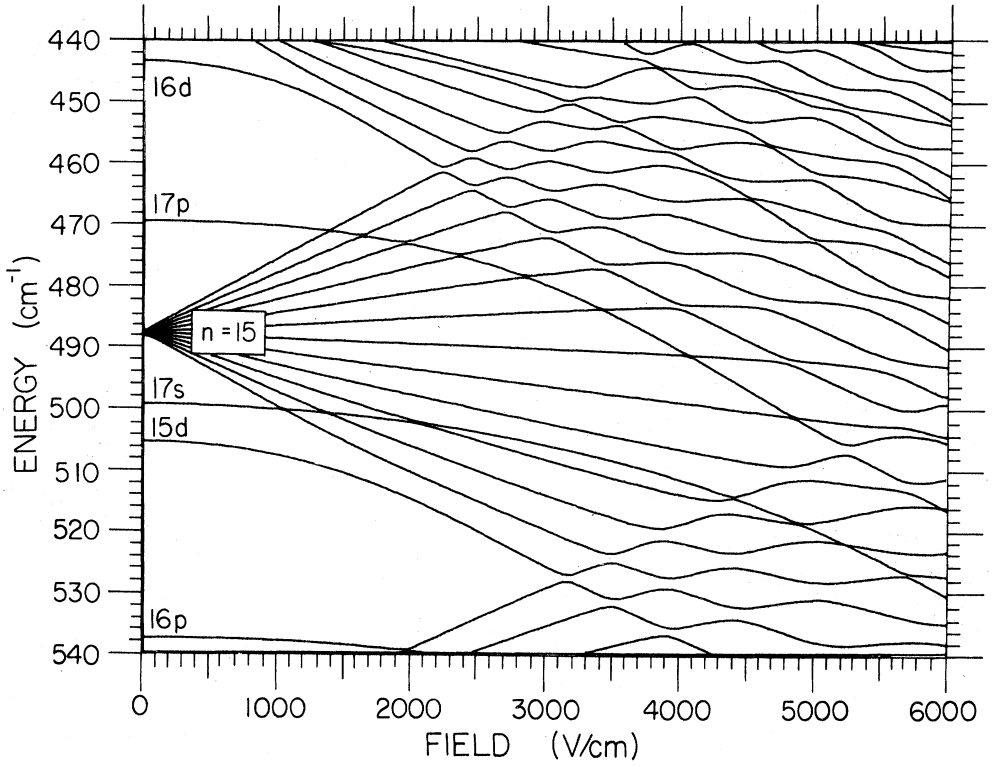

FIG. 14. Potassium, $m = 0$.

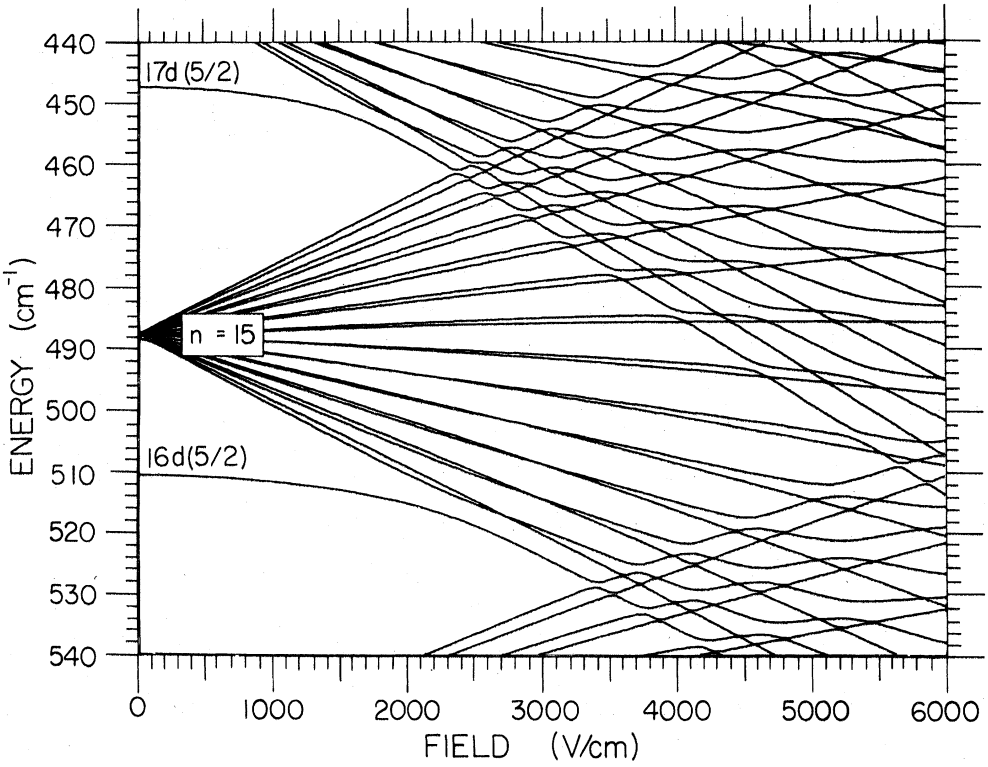

FIG. 15. Rubidium, $|m_j| = \frac{5}{2}$. J indicated in parentheses.

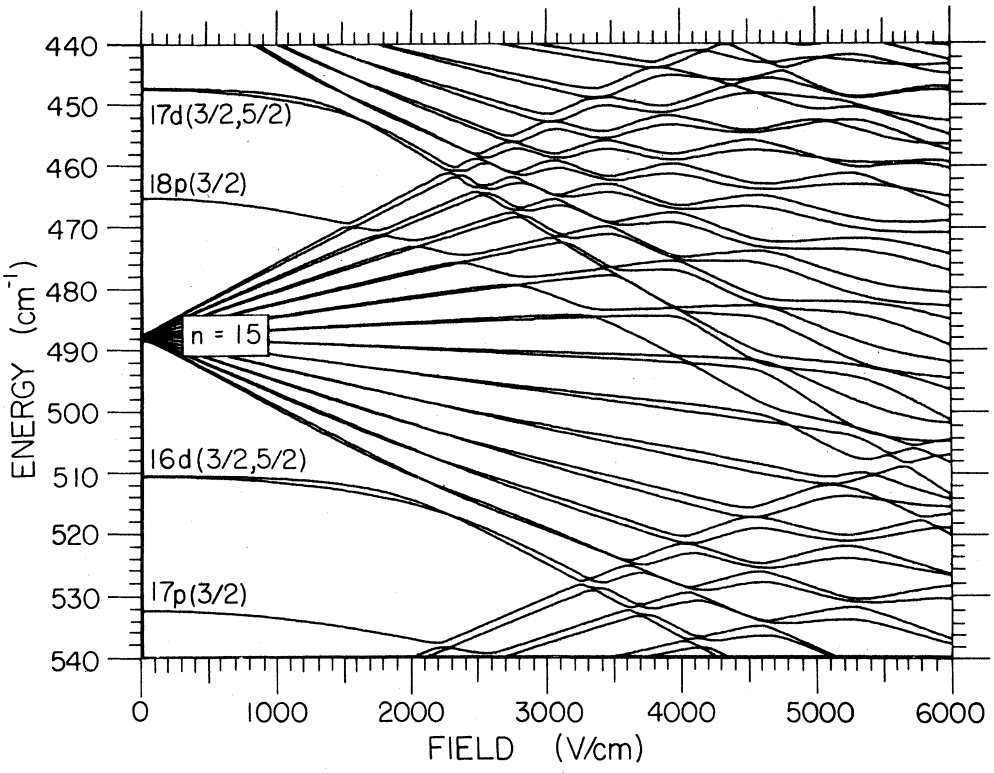

FIG. 16. Rubidium, $|m_j| = \frac{3}{2}$.

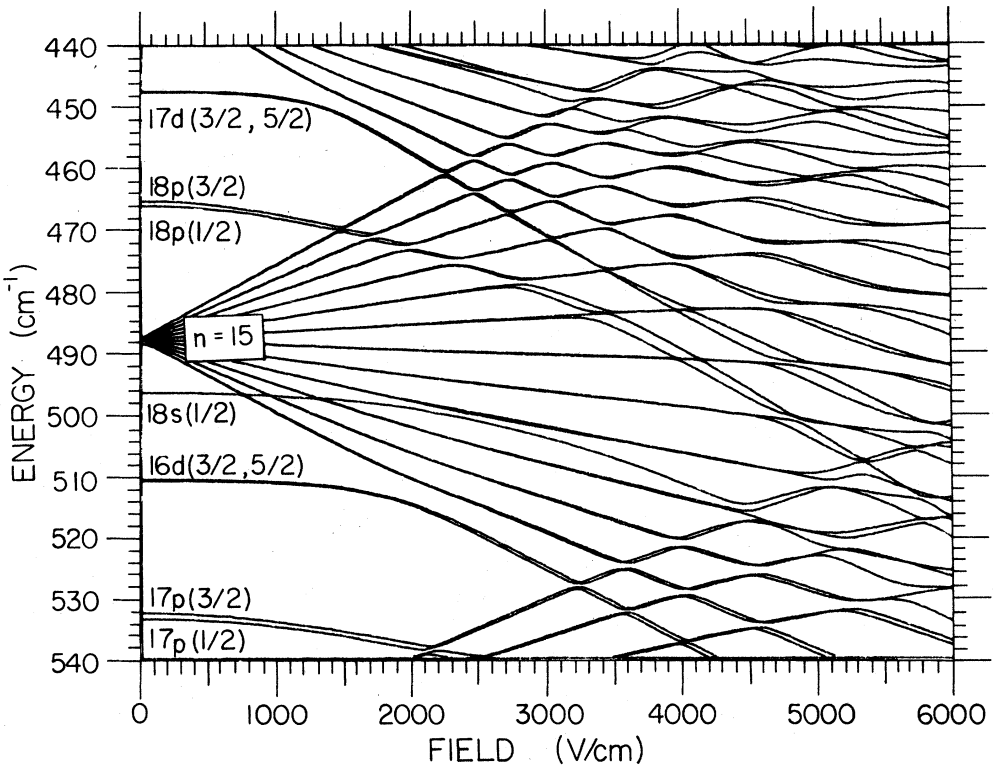

FIG. 17. Rubidium, $|m_j| = \frac{1}{2}$.

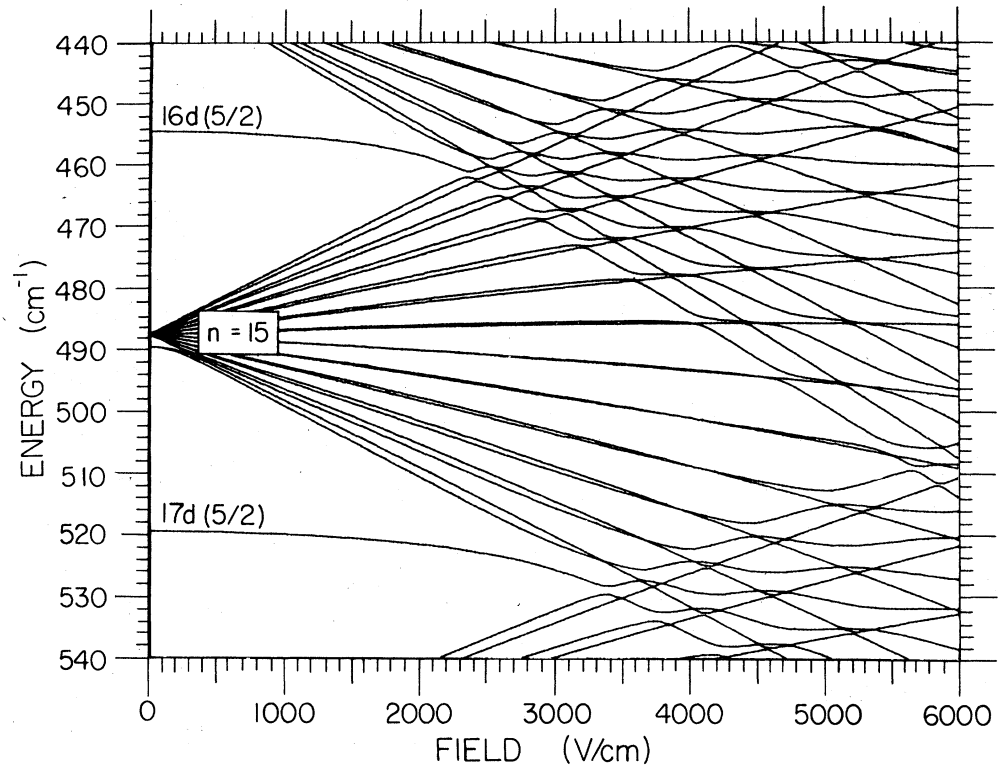

FIG. 18. Cesium, $|m_j| = \frac{5}{2}$.

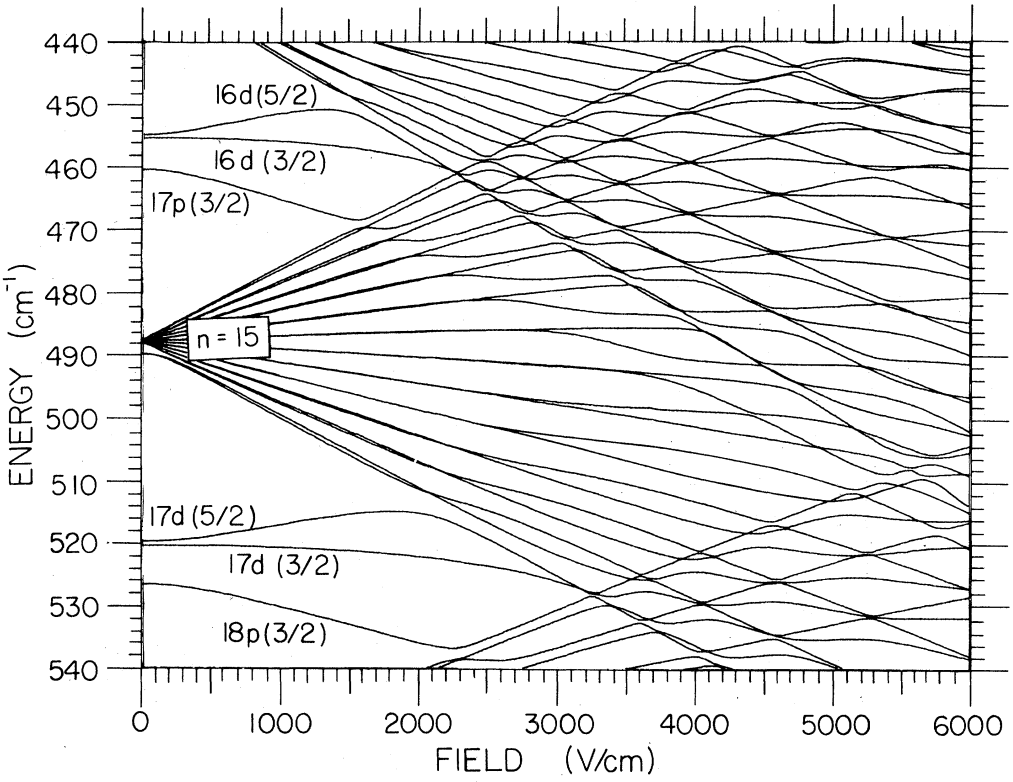

FIG. 19. Cesium, $|m_j| = \frac{3}{2}$.

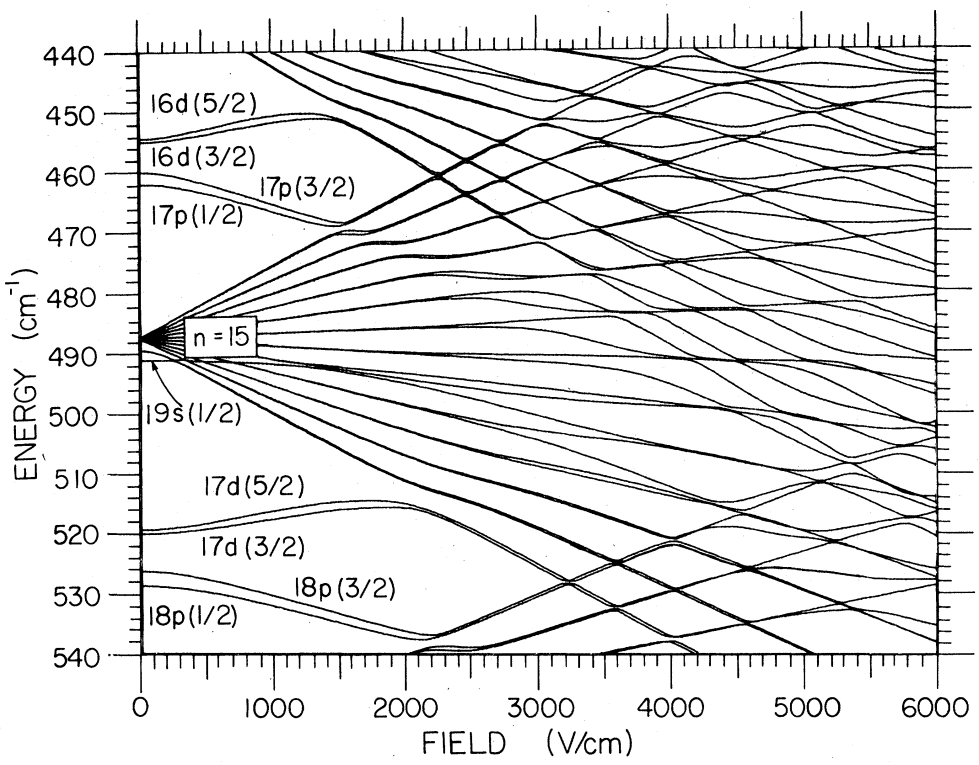

FIG. 20. Cesium, $|m_j| = \frac{1}{2}$.

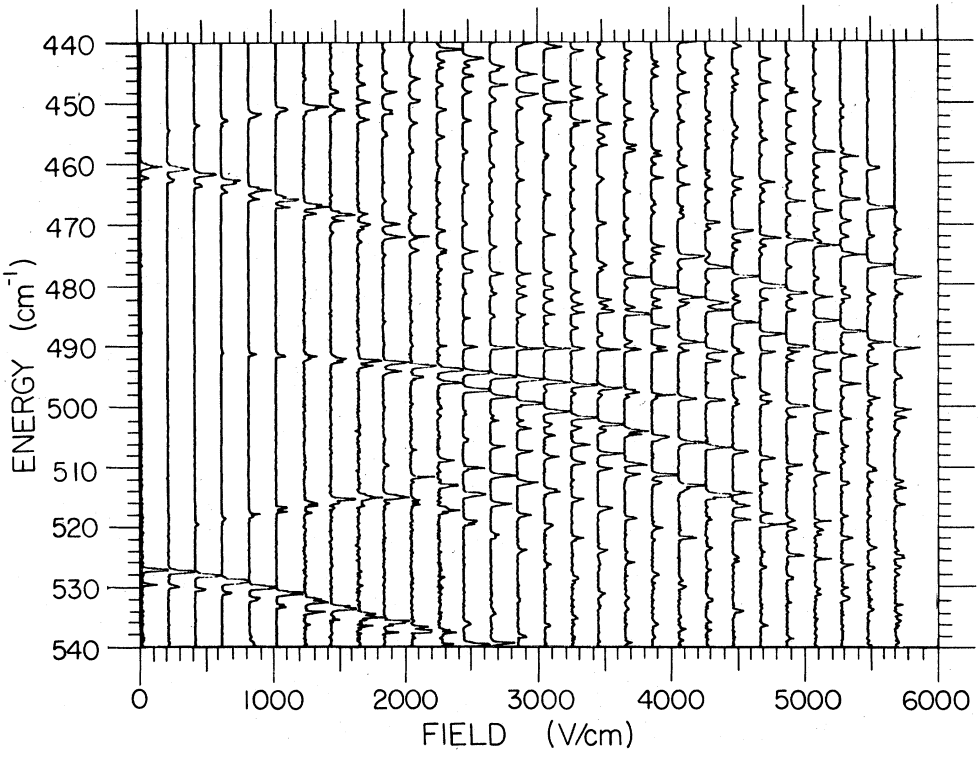

FIG. 21. Cesium, $|m_j| = \frac{1}{2}$; experimental Stark structure.

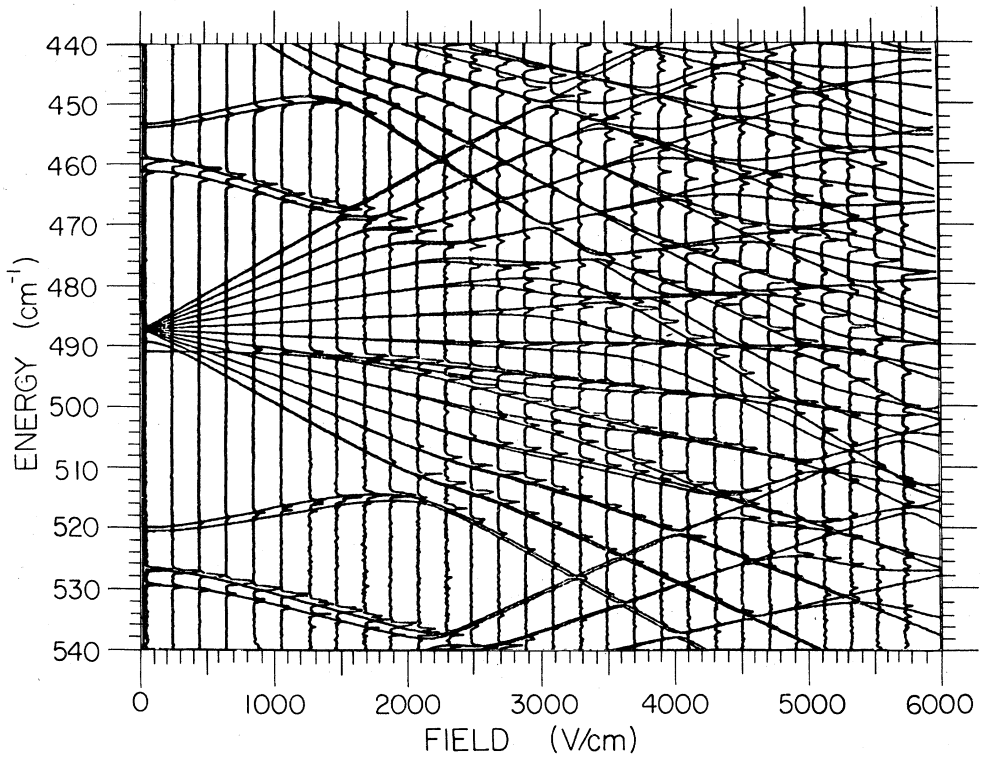

FIG. 22. Cesium, $|m_j| = \frac{1}{2}$; calculated and experimental Stark structure.

dicted by our calculations are not artifacts of using a truncated basis set.

B. Experimental map of a level crossing

As a further check of the accuracy of our calculations we have mapped the avoided crossing between two $|m| = 1$ levels of lithium: the intersection of (18, 16, 0, 1) and (19, 1, 16, 1) at 321.5 cm^{-1}, 843 V/cm. The experimental procedure is similar to that described above except that a pulse-amplified cw dye laser was used to excite the final step. The spectral resolution was approximately 0.01 cm^{-1}. The results are shown in Fig. 23. The levels are actually doublets due to the hyperfine splitting in the 3s state, but the doublet splitting is not fully resolved. An interesting feature of the data is that one level disappears at the anticrossing while the other becomes twice as intense. Away from the crossing the oscillator strengths to the two states are approximately equal. The eigenstates at the anticrossing are the symmetric and antisymmetric combination of these states, so that the oscillator strength is transferred completely to one state.

The calculated level structure is superimposed on the data. The calculated separation is 0.072 cm^{-1}, while the measured separation is 0.072(5) cm^{-1}. To ensure that this agreement was not simply fortuitous we also mapped the crossing at 321.8 cm^{-1}, 1531 V/cm. The calculated separation was 0.204 cm^{-1}, while the observed separation was 0.207(6) cm^{-1}. These results suggest that anticrossings in the alkali metal can be calculated reliably to within at least 0.01 cm^{-1}.

TABLE V. Calculated level separation at apparent anticrossing. Intersection of hydrogenic levels (15,14,0,0) and (16,0,15,0).

Basis set	Field (V/cm)	Energy (cm^{-1})	Separation (cm^{-1})
$n=14$–16	2042.15	459.854	2×10^{-4}
$n=13$–18	2043.45	460.592	4×10^{-4}
$n=13$–20	2043.40	460.603	5×10^{-4}
Perturbation theory	2043.35	460.601	0

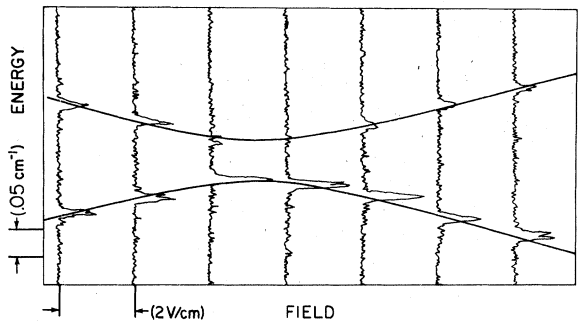

FIG. 23. Level anticrossing in lithium. Intersection of state (18,16,0,1) and (19,1,16,1) at 321.5 cm^{-1}, 943 V/cm. The calculated level structure is superimposed on the data.

C. Anticrossings in one-electron atoms

We expect that level separations at anticrossings in one-electron atoms should be sensitive functions of the quantum defects, vanishing as the quantum defects approach zero and the system becomes hydrogenic. The Stark maps in Sec. VI suggest that this is the case. In general, large fractional quantum defects produce large level repulsions. Compare, for instance, the Stark maps for Na $m=0$ and $|m|=1$ states. For $m=0$ (Fig. 11) the quantum defects are $\delta_0=1.35$ and $\delta_1=0.84$. (The remaining defects are close to zero.) For $|m|=1$, Fig. 10, the only large defect is $\delta_1=0.84$. The level repulsions are markedly stronger for the case $|m|=0$. This behavior is typical.

Unfortunately, it is difficult to generalize about the structure of anticrossings for states with several large quantum defects. Although repulsions are generally strong, they can suddenly diminish, producing unexpected pseudocrossings. One such case has been noted for lithium $m=0$ (Fig. 6) at 4.8 kV/cm, 507 cm^{-1}. Under certain conditions another interesting feature may be present; a single level may "cross" levels from a nearby Stark manifold. Such a feature for potassium can be seen in Fig. 12 near 4.6 kV/cm, 455 cm^{-1}.

In situations where only a single quantum defect differs from zero it is possible to provide a general characterization of the anticrossings. For example, consider the first anticrossing between the manifold n and $n+1$. This occurs between the states $(n, n-1, 0, 0)$ and $(n+1, 0, n, 0)$ at a field $F \cong 1/3n^5$. The average density of $m=0$ Stark states is $dn/dE = n^4$, and since the maximum possible level repulsion is one half the separation between states, the natural unit for measuring level repulsions is the mean separation, $1/n^4$.

In Fig. 24 we show the magnitude of level separations calculated for the first anticrossing between the n and $n+1$ manifold, $m=0$, as a function of the s-state quantum defect. As expected, the separation vanishes as $\delta_0 \to 0$ or $\delta_0 \to 1$. For small defects the separation varies linearly with δ according to $\Delta W = (1.9/n^4)\delta$. This relation is obeyed accurately for $n=15, 16$ and $n=25, 26$, which suggests that the curve may be universal.

VIII. REMARKS

In this paper we have focused exclusively on the energy range in the vicinity of $n=15$. The application of our methods for calculating alkali-metal Stark structure to other energy regions is straightforward, and the only reliable way to predict the Stark structure in a particular region of energy and field is to carry out such a calculation. Certain qualitative features, however, can be extrapolated from our results thanks to the constancy of the quantum defects. For instance, the intrusion of the rubidium s and p states into the linear manifold discussed in Sec. VI D will occur for all values of n. The size of the level anticrossings for a small quantum defect has been shown to obey a simple n^{-4} scaling law. Other scaling laws are easily determined. The density of Stark states scales as n^4 for $m=0$ and n^3 for $|m|=n-1$. The field for the initial crossing between two manifolds scales as n^{-5}, the field for the onset of field ionization scales as n^{-4}, and the number of crossings before a given level reaches the threshold for ionization scales as n^2 for $m=0$ and as n for $|m|=n-1$. If the high-field Stark states form a strongly interacting manifold for one range of energy, as in the case of Na $m=0$ (Fig. 11), they can be expected to behave similarly for all values.

The scaling laws are helpful in predicting qualitative features of the Stark structure in uncharted regions, but they must be used with caution. For example, the accidental degeneracies, or "sharp crossings," in the midst of a set of strongly repelling lines do not appear to obey any simple scaling law. Such degeneracies can cause confusion in the identification of a level or lead to unexpected nonadiabatic effects in the presence of a time-varying field.

Our goal of accuracy, 0.05 cm^{-1}, is not ambitious in the context of modern spectroscopy, though it is entirely adequate for the principle application: the reliable identification of completely resolved Stark states in an arbitrary field. It should be realized, however, that the potential accuracy is very high. For instance, relative energy separations as judged by level separations at anticrossings appear to be accurate to 5×10^{-4} cm^{-1}, as discussed in Sec. VII. Furthermore, the major error, perturbations due to states excluded from the basis set, decreases rapidly with de-

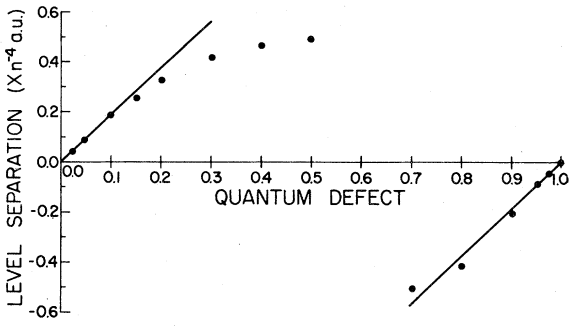

FIG. 24. Calculated level separation vs quantum defect for the first anticrossing between terms n and $n+1$. Solid line is given by $\Delta W = 1.9\delta/n^4$.

creasing field. If higher accuracy is desired, the most straightforward course is simply to expand the basis set. Alternatively, the effect of nondegenerate states can be taken into account by perturbation theory once the system has been diagonalized. In any case, the importance of the truncation error can be revealed by varying the size of the basis set, providing a reliable procedure for judging the accuracy of a particular calculation.

The ability to calculate Coulombic matrix elements accurately and efficiently has numerous applications beyond the problem of alkali-metal Stark structure. For example, our methods have been applied successfully to the calculation of the diamagnetic energy of Rydberg atoms in a strong magnetic field.[19] Also, the method can be applied to two-electron systems by using multichannel quantum-defect theory to identify the correct configurations. One example of this—the Stark structure of barium for Rydberg levels in the vicinity of a doubly excited state—has been previously reported.[20]

This study has provided a number of insights into Stark structure. For instance, it has revealed qualitative features which were quite unpredicted, such as the strong nonhydrogenic structure induced by a single large quantum defect or the accidental degeneracies in high fields. In some respects, however, our understanding is incomplete. Diagonalization of the energy matrix, treating the field as a perturbation, may not be the best approach. The physics of alkali-metal Stark structure is completely determined by the quantum defects, so that in principle one should be able to predict the structure directly from them. This suggests that it may be better to calculate the Stark structure in a parabolic representation and then treat the effect of the core as a perturbation.

The major goals of this work have been to develop practical methods for calculating alkali-metal Stark structure with sufficient accuracy to allow every level to be unambiguously identified, to provide a comprehensive collection of Stark maps of the alkali metals, and to obtain insights into the systematics of Stark structure. We believe that these goals have been substantially accomplished.

ACKNOWLEDGMENTS

We thank Richard R. Freeman for helpful discussions and William D. Phillips, Mark D. Havey, and W. Mark Finlay for assistance in the measurements of the level anticrossings. This work was sponsored by the National Science Foundation under Grant No. PHY-77-09155; one of us (M.M.K.) was the recipient of a NSF Graduate Fellowship.

APPENDIX A. EVALUATING RADIAL-MATRIX ELEMENTS

We have calculated the radial-matrix element $\langle nl|r^{\sigma}|n'l'\rangle$, $\sigma \geq 0$, for nonhydrogenic one-electron Rydberg states by generalizing the Coulombic wave functions to nonintegral n, and also by numerically integrating the radial wave equation with a general central potential. The calculations presented in this paper employed numerical integration because it is less susceptible to roundoff errors for large values of $n-l$ than the polynomial method and because non-Coulombic potential terms can be added to account for effects of fine structure ($V \sim r^{-3}$) or core polarization ($V \sim r^{-4}$). In some cases, however, the polynomial expansion is convenient to use. In particular, for $n-l \lesssim 12$, it is faster and more accurate than numerical integration. For completeness we shall describe both methods. Note that the phase convention for the radial wave function R is $R(r \to \infty) \to 0^+$. [The usual phase convention is the sign of $R(r \to \infty) = (-1)^l$.]

A. Polynomial expansion

The polynomial expansion for Coulombic wave functions proceeds directly from the radial wave equation.[1] Taking $\epsilon = \sqrt{-2W}$ and $R(r) = \exp(-\epsilon r) f(r)$, we obtain

$$f'' + 2(1/r - \epsilon) f' + \left(2\frac{Z-\epsilon}{r} - \frac{l(l+1)}{r^2}\right) f = 0 .$$

We can expand f in the form

$$f = \sum_{v=0}^{\infty} a_v r^{\lambda - v} .$$

(Note that f is written as a *decreasing* power series in r.) For R to be normalizable the power series must terminate. Solving for λ and a_v yields the relations

$$\lambda = Z/\epsilon - 1 = n - 1 ,$$

$$W = -Z^2/2n^2 ,$$

$$a_v = -a_{v-1}(n/2Z)(n-l-v)(n-v+l+1)/v .$$

The series terminates when $v = n-l-1$, provided that n is an integer. It explicitly satisfies the inner boundary condition that R be finite as $r \to 0$. The series is related to the associated Laguerre polynomial $L_j^k(r)$:

$$r^l L_{n+l}^{2l+1} \propto (-1)^{n-l} \sum_{v=0}^{n-l-1} a_v r^{n-v-1} .$$

If the energy W is allowed to become nonhydrogenic, n becomes nonintegral, the series fails to terminate, and the inner boundary condition is no longer satisfied. This is to be expected, for the $1/r$ potential is incorrect within the core of inner electrons near the origin and the wave function cannot be Coulombic in that region. The radius of the core, however, is small compared to n^2, the radius of the Rydberg electron. Thus the series can be terminated with the same number of nodes or terms as for hydrogen. Writing $n^* = n - \delta_l$, where δ_l is the quantum defect and n is an integer, the number of terms in the series is the integer of $n^* + \frac{1}{2}$.

Calculating the matrix element of r^σ between two states n, l and n', l' and normalizing by putting $\sigma = 0$ yields

$$\langle nl|r^\sigma|n'l'\rangle = G(\sigma)_{n'l'}^{nl}[G(0)_{nl}^{nl} G(0)_{n'l'}^{n'l'}]^{-1/2} ,$$

where

$$G(\sigma)_{n'l'}^{nl} = \sum_v \sum_{v'} a_v a_{v'}' \int_0^\infty e^{-Ar} r^{n+n'-v-v'+\sigma} dr$$

$$= \sum_v \sum_{v'} a_v a_{v'}' \frac{\Gamma(n+n'-v-v'+\sigma+1)}{A^{(n+n'-v-v'+\sigma+1)}} .$$

Here $v = 0, 1, \ldots, n-l-1$, $v' = 0, 1, \ldots, n'-l'-1$, and $A = 1/n + 1/n'$. To evaluate these expressions numerically the terms must be arranged to prevent large numbers from appearing in the factorials. The major source of error arises from taking small differences between large alternating terms in the series. With 16 decimal digits of precision, the error for $n-l = 10$ is less than 10^{-6}. For $n-l = 18$ the error is 10%, and beyond that it diverges.

The method can be applied to higher values of n by using extended precision but only at great cost in computer time.[21] Because of this, and because the polynomial method is incapable of dealing with non-Coulombic terms in the potential, we have chosen to generate the matrix elements by numerical integration.

B. Numerical integration

When numerically solving differential equations with oscillating solutions, it is desirable for the number of grid points per oscillation to be approximately constant. The period of a Coulombic wave function increases rapidly with r, so that either a nonuniform grid spacing or a change of variable is needed. The fastest and most accurate method that we have tested is based on the Numerov algorithim with a logarithmic scaling variable.[22] Taking $x = \ln r$ and letting $X = r^{1/2}R$, the radial equation takes the standard Numerov form

$$\frac{d^2X}{dx^2} = g(x)X ,$$

where $g(x) = 2e^{2x}[V(x) - E] + (l+\frac{1}{2})^2$.

If we let $r_j = r_s \exp(-jh)$, where h is the logarithmic step size, the Numerov algorithim is

$$X_{i+1} = \left[X_{i-1}\left(g_{i-1} - \frac{12}{h^2}\right) + X_i\left(10g_i + \frac{24}{h^2}\right)\right] \Big/ \left(\frac{12}{h^2} - g_{i+1}\right) .$$

The matrix element of r^σ is

$$\langle E, l\,|r^\sigma|E', l'\rangle = \sum_i X_i X_i' r_i^{2+\sigma} \left(\sum_i X_i^2 r_i^2 \sum_j X_j'^2 r_j^2\right)^{-1/2} .$$

The integration is executed in the inward direction because only the outer boundary condition is known and because this procedure minimizes cumulative numerical errors at large r, where the major contributions to the matrix elements occur. The step size for all the calculations is 0.01. The starting point r_s is determined by the requirement that $R(r_s) \cong 10^{-10} R(r_0)$, where r_0 is the outer turning point. Typical values are $r_0 = 2n^2$ and $r_s = 2n(n+15)$. The initial slope of the wave function is taken to be that of a decreasing exponential. (The integration is insensitive to the initial values because admixtures of the incorrect solution damp out exponentially.)

The integration terminates at an inner value of r which, for low l states, is taken to be the core radius given by (polarizability)$^{1/3}$. (For hydrogen the core radius is taken to be 0.05.) For higher l states the integration is carried past the inner turning point and terminated when the solution starts to diverge.

To check the accuracy of the numerical integration we have compared the dipole-matrix elements for hydrogen to the exact result $\langle n, l\,|r|n, l-1\rangle = \frac{3}{2}n(n^2 - l^2)^{1/2}$. The results are shown in Table VI.

For low values of n the error is due primarily to the inner cutoff at $r = 0.05$. As n increases this error rapidly decreases, but as the number of nodes and grid points become large, numerical integration errors start to grow and the error in

TABLE VI. Integration error of $\langle n,l\,|\,r\,|\,n,l-1\rangle$.

n	l	Exact result (a.u.)	Fractional error
10	1	149.248	2.6×10^{-5}
10	9	65.384	1.8×10^{-6}
20	1	599.250	2.7×10^{-6}
20	19	187.350	1.6×10^{-6}
50	1	3749.250	5.5×10^{-5}
50	49	746.241	7.6×10^{-6}

the matrix elements increases. For a fixed value of n the error decreases as l becomes larger due to the shorter integration range and the smaller number of nodes. It should be noted that the logarithmic grid variable is not strictly correct. For a fixed grid size the number of grids points per outer node becomes smaller as n increases. If there are less than a few points per node, the error decreases. The numerical values used here have been optimized for $n\cong15$, the primary area of interest in this paper, though the methods can work well at much larger values of n.

APPENDIX B. DIAGONALIZATION PROCEDURE AND ERRORS

The energy matrices were diagonalized using the Jacobi diagonalization method adapted for digital computers by Von Neumann,[23] with a modified convergence test. Although faster and perhaps more accurate methods exist for this type of diagonalization, the Jacobi method had the advantage of requiring a minimum of computer memory.

The Jacobi method is based on repeated diagonalization of the 2×2 submatrix which currently has the largest off-diagonal matrix element. The diagonalization is terminated when all off-diagonal matrix elements are less than a threshold value. In our calculations the threshold was taken to be 0.05 cm^{-1}. The maximum eigenvalue error due to incomplete diagonalization is $\sqrt{s-1}$ times the threshold value, where s is the number of states, but a more realistic estimate of the error can be obtained by treating the residual off-diagonal matrix elements as a perturbation. (The residual matrix elements are evaluated after the numerical diagonalization is terminated.) For an isolated eigenstate the error is second order and varies as the square of threshold. In our region of study the maximum error for a well isolated eigenstate is about 0.002 cm^{-1}, though in many cases it is substantially less because of cancellations among residual matrix elements for states above and below the isolated eigenstate. If two eigenstates are almost degenerate, as in the case of sharp anticrossings, the error is less than 0.05 cm^{-1}. The error for hydrogen is found to be 5×10^{-4} cm^{-1}. If all the eigenstates are degenerate and all the off-diagonal matrix elements are at threshold, then the worst case result described above could be realized.

APPENDIX C. SOME COMPUTATIONAL CONSIDERATIONS

Our calculations were carried out on a PDP 11/34 minicomputer with floating-point hardware. The average instruction time is 3 μsec and the "multiply" instruction time is 13 μsec. The time to calculate a single matrix element varies from 0.7 sec for $\langle10,9\,|r\,|10,8\rangle$ to 1.3 sec for $\langle10,0\,|r\,|10,1\rangle$. At $n=100, l=0$ the time is 2.1 sec. Approximately 11 min is required to calculate all matrix elements in the range $n=13$–20. The diagonalization time for this basis is approximately $t=370\,\text{sec}\times[E(\text{kV/cm})]^{0.36}$. The time varies with the size of the basic set s roughly as s^2. The total time to diagonalize all field points from 0 to 6 kV/cm in 100 V/cm steps is approximately 8 h.

There are a number of ways to speed the computations. A faster computer or an array processor could decrease the time by factors up to several hundred. Time-efficient diagonalization algorithms could further decrease the computation time at the expense of memory. A substantial improvement could be realized by using the eigenvectors at a given field point to recalculate the matrix elements for an adjacent field point. Thus, instead of independently diagonalizing at each field point, the results of each diagonalization are used to start the next. Symbolically this can be written

$$\bar{\bar{W}}_j=\bar{\bar{U}}_j^{-1}[\bar{\bar{W}}_{j-1}+\Delta F(\bar{\bar{U}}_{j-1}^{-1}\cdots\bar{\bar{U}}_1^{-1}\bar{\bar{Z}}\,\bar{\bar{U}}_1\cdots\bar{\bar{U}}_{j-1})]\bar{\bar{U}}_j\,,$$

where $\bar{\bar{Z}}$ is the perturbation matrix in the spherical basis and $\bar{\bar{U}}$ is the unitary transformation which diagonalizes the energy matrix $\bar{\bar{W}}$. This can be reduced to the familiar result:

$$\bar{\bar{W}}_j=\bar{\bar{U}}_j^{-1}\cdots\bar{\bar{U}}_1^{-1}(\bar{\bar{W}}_0+\sum_j\Delta F\bar{\bar{Z}})\bar{\bar{U}}_1\cdots\bar{\bar{U}}_j$$

$$=\bar{\bar{U}}^{-1}(\bar{\bar{H}}_0+F\bar{\bar{Z}})\bar{\bar{U}}\,.$$

[1]H. A. Bethe and E. E. Salpeter, *Quantum Mechanics of One- and Two-Electron Atoms* (Academic, New York, 1957).
[2]H. J. Silverstone, Phys. Rev. A 18, 1853 (1978).
[3]P. M. Koch, Phys. Rev. Lett. 41, 99 (1978); I. W. Herbst and B. Simon, *ibid.* 41, 67 (1978).
[4]M. G. Littman, M. M. Kash, and D. Kleppner, Phys. Rev. Lett. 41, 103 (1978).

[5]K. Helfrich, Theor. Chim. Acta 24, 271 (1972).
[6]D. R. Bates and A. Damgaard, Philos. Trans. R. Soc. London 242, 101 (1949).
[7]D. R. Herrick, Phys. Rev. A 12, 1949 (1975), and references therein.
[8]R. R. Freeman and D. Kleppner, Phys. Rev. A 14, 1614 (1976).
[9]R. F. Stebbing, C. J. Lattimer, W. P. West, F. B. Dunning, and T. B. Cooke, Phys. Rev. A 12, 1453 (1975); T. W. Ducas, M. G. Littman, R. R. Freeman, and D. Kleppner, Phys. Rev. Lett. 35, 366 (1975).
[10]M. G. Littman and H. J. Metcalf, Appl. Opt. 17, 2224 (1978); I. Shoshan, N. Danon, and V. Oppenheim, J. Appl. Phys. 48, 4495 (1977).
[11]C. E. Moore, *Atomic Energy Levels*, NSRDS-NBS 35 (U.S. GPO, Washington, D. C., 1971).
[12]C. Fabre, S. Haroche, and P. Goy, Phys. Rev. A 18, 229 (1978).
[13]C. Corliss and W. C. Martin, NBS (private communication).
[14]K. B. S. Eriksson and I. Wenäker, Phys. Scr. 1, 21 (1970).
[15]D. Popescu, M. L. Pascu, C. B. Collins, B. W. Johnson, and I. Popescu, Phys. Rev. A 8, 1666 (1973).
[16]U. Litzén, Phys. Scr. 1, 253 (1970).
[17]M. G. Littman, M. L. Zimmerman, T. W. Ducas, R. R. Freeman, and D. Kleppner, Phys. Rev. Lett. 36, 788 (1976).
[18]G. J. Hatton, Phys. Rev. A 14, 1083 (1978).
[19]M. L. Zimmerman, J. C. Castro, and D. Kleppner, Phys. Rev. Lett. 40, 1083 (1978).
[20]M. L. Zimmerman, T. W. Ducas, M. G. Littman, and D. Kleppner, J. Phys. B 11, L11 (1978).
[21]F. Gounand, J. Phys. (Paris) 40, 457 (1979), and references therein.
[22]C. Froese, Can. J. Phys. 41, 1895 (1963); J. M. Blatt, J. Comput. Phys. 1, 378 (1967).
[23]*Mathematical Methods for Digital Computers*, edited by A. Ralston and H. S. Wilf (Wiley, New York, 1962), Chap. 7.